UNIVERSITY OF OKLAHOMA

GRADUATE COLLEGE

SENSITIVITY OF VORTEX PRODUCTION TO SMALL ENVIRONMENTAL PERTURBATIONS IN HIGH-RESOLUTION SUPERCELL SIMULATIONS

A THESIS

SUBMITTED TO THE GRADUATE FACULTY

in partial fulfillment of the requirements for the

Degree of

MASTER OF SCIENCE IN METEOROLOGY

By

BRITTANY ANNE DAHL
Norman, Oklahoma
2014

SENSITIVITY OF VORTEX PRODUCTION TO SMALL ENVIRONMENTAL PERTURBATIONS IN HIGH-RESOLUTION SUPERCELL SIMULATIONS

A THESIS APPROVED FOR THE
SCHOOL OF METEOROLOGY

BY

_____
Dr. Amy McGovern, Chair

_____
Dr. Rodger Brown, Co-Chair

_____
Dr. Kelvin Droegemeier

_____
Dr. Louis Wicker

Acknowledgements

None of this would have been possible without the many people who have supported me along the way. First, I want to thank the members of my thesis committee for their contributions and encouragement throughout the research process. My advisor, Dr. Amy McGovern, provided access to the needed supercomputing tools and provided several opportunities for me to share my work. Dr. Lou Wicker greatly assisted with both the atmospheric modeling side and formulating the idea behind this project. Dr. Rodger Brown also shared many good suggestions as I worked on this project. Finally, I am grateful to Dr. Kelvin Droegemeier for taking time out of his very busy schedule to participate in my committee and lend his perspective.

Several other colleagues assisted me in various aspects of research. Dr. Corey Potvin allowed me to use his code for the vortex detection algorithm and provided useful comments as I analyzed the data. Dr. Leigh Orf's expertise with running the CM1 model in MPI and Dr. Ted Mansell's expertise with the microphysics parameterizations in the model were much appreciated.

I am grateful to my friends and family for their encouragement and emotional support as I completed this degree. In particular, I want to thank my parents, Pete and Jane Benson, for always believing in me and indulging me as a child when all I wanted to do was watch The Weather Channel. I am also forever appreciative of my fellow meteorologist and husband, Nathan Dahl, who has been a constant source of strength through it all.

This project was funded by NSF Information & Intelligent Systems grant 0746816 and the NOAA Warn-on-Forecast Project. Supercomputing resources were

provided through XSEDE allocation TG-ATM090047. The storm simulations and data extraction were performed and Kraken and Darter, and visualization were created on Nautilus, all of which are maintained by the University of Tennessee and Oak Ridge National Laboratory's Joint Institute for Computational Sciences. The vortex detection algorithm was run on Stampede, which is maintained by the Texas Advanced Computing Center at the University of Texas at Austin.

Table of Contents

List of Tables

List of Figures

Abstract

Studies have indicated that both initial condition and model errors within atmospheric models can propagate upscale as well as downscale, which limits the range of practical predictability in numerical forecasts (Hohenegger and Schär 2012). With short-term storm-scale prediction to play an increasingly important role in tornado warning operations (e.g., Warn-on-Forecast), it is beneficial to understand the relative impact of errors from the background mesoscale environment on fine-scale features associated with supercell tornadogenesis.

To investigate the effect of relatively small mesoscale errors on submesocyclone-scale vortex development in simulated supercells, perturbations are randomly drawn from typical 1-hour forecast errors observed from the 13 km RUC model and applied to the 29 May 2004 Geary, OK sounding using the method of Cintineo and Stensrud (2013). Three sounding ensembles are created by scaling these errors to 10%, 25%, and 50% of their original magnitude. These are then used to initialize horizontally homogeneous environments for three sets of 20 idealized simulations at a horizontal resolution of 100 m (plus a control forecast). The Vortex Detection and Classification (VDAC) algorithm outlined in Potvin (2013) was used to identify vertically continuous submesocyclone-scale vortices. Finally, a case study was conducted between six members of the 50% perturbation ensemble to examine specific impacts of environmental conditions on processes related to vortex development.

Statistical analysis of vortices detected by the algorithm showed that the distribution of total detections per ensemble member were not statistically different in the 10% and 25% ensembles, suggesting that there may be a threshold in error reduction

beyond which improved analysis of the background mesoscale state in which the storm forms will not improve forecasts. However, reducing the initial state errors may improve the prediction of the spatial "envelope" in which the vortices occur. The spread of vortex locations perpendicular to the storm path as well as the length of time over which vortices develop decrease as the initial error magnitude decreases. Distributions of observed vortex tangential velocity and radius differed between ensembles without a clear pattern, although ensemble maxima of these characteristics appear to be correlated with the LCL, LFC, CAPE, and CIN of the initial environment. The results of the case study suggest that location and intensity of cold pools near the rear flank, which appear to be correlated to a slight reduction in low-level moisture, may be responsible for significant changes in overall vortex statistics in certain realizations.

Chapter 1: Introduction

Tornadoes associated with supercell thunderstorms pose a significant threat to life and property. Initiatives such as Warn-on-Forecast (Stensrud et al. 2009, 2012) seek to improve the accuracy of tornado forecasts and extend the lead-time of warnings through use of short-term, storm-scale numerical weather prediction. However, tornadoes are difficult to predict due to their size and their relatively short life span.

Predictability theory indicates that errors in the initial conditions of numerical models grow exponentially with time, which limits the range of practical predictability for atmospheric phenomena. In the context of tornado prediction, errors in the storm environment propagate downscale toward storm-scale processes, including those that contribute to low-level mesocyclogenesis. A greater understanding of the sensitivity of model forecasts of low-level mesocyclones to relatively small changes in the environment is therefore important. Cintineo and Stensrud (2013, hereafter CS13) investigated the impact of typical errors within convective environments in RUC (Rapid Update Cycle) model forecasts on the predictability of supercell features modeled at 1 km horizontal resolution. This study builds upon their work by increasing the resolution to 100 m in order to examine the sensitivity of submesocyclone-scale vortex generation to smaller environmental perturbations than those employed in CS13.

Chapter 2 contains a review of literature pertaining to the development of low-level rotation in supercells, numerical modeling of supercells, and predictability theory. Chapter 3 describes the method of generating perturbations in the environmental soundings, characteristics of three ensembles of perturbed soundings, settings used in the atmospheric model, and details of the vortex detection algorithm used to locate low-

level vortices in the wind field. Chapter 4 presents an analysis of the characteristics of vortices detected in the simulations, the relationship between vortex characteristics and the initial environment, and a case study of selected ensemble members to examine the relationship between storm environment and storm processes that contribute to the development of low-level rotation. Chapter 5 concludes with a discussion of the results and topics for future study.

Chapter 2: Background

2.1 Overview of Supercell Thunderstorms

2.1.1 Development of Midlevel Rotation

Supercell thunderstorms are characterized by a deep, rotating updraft, known as a mesocyclone, and tend to be relatively longer lived than ordinary single cell thunderstorms (Browning 1964; Doswell and Burgess 1993). Both buoyancy and the presence of deep vertical wind shear are crucial to storm development. Strong rotation in tornadic supercells initially develops in the midlevels before becoming apparent at lower levels (Klemp and Rotunno 1983). The main mechanism responsible for this rotation is the tilting and stretching of horizontal vorticity into the vertical by the horizontal gradient in vertical motion (Rotunno 1981; Davies-Jones 1984; Klemp 1987).

Midlevel rotation can be enhanced by favorable changes in the direction of the shear vector with height. Environmental vortex lines are arched upward as they are advected by the updraft and form a vertical vorticity couplet on either side of the updraft (Davies-Jones 1984). If the storm-relative wind and the environmental vorticity vectors are aligned with one another (i.e., streamwise vorticity is present, as in Figure 1), this results in a correlation between the locations of the positive vorticity and vertical velocity maxima, which leads to stretching and intensification of midlevel rotation in the updraft. The environment in Figure 1 would favor a cyclonically rotating updraft because the vorticity vector is streamwise with height.

Baroclinically generated horizontal vorticity can also be found along the forward flank gust front as the evaporation of hydrometeors leads to the development of a

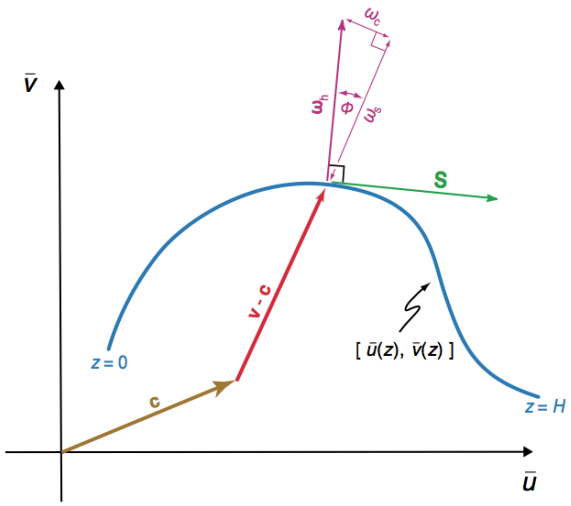

Figure 5. Cyclonically curved example hodograph (blue) including vectors for storm motion (c), storm-relative environmental wind (v-c), shear (S), and environmental horizontal vorticity (ω_h) with streamwise (ω_s) and crosswise (ω_c) components. (From Markowski and Richardson 2010, Fig. 2.12)

horizontal buoyancy gradient at low levels (Figure 2; Klemp and Rotunno 1983). This is a particularly rich source of streamwise vorticity to be ingested by the storm's updraft if the storm-relative inflow winds are oriented parallel to this boundary. The resulting inflow parcels are then tilted and stretched by the storm's updraft.

2.1.2 Low-level Rotation Preceding Tornadogenesis

Prior to tornadogenesis, strong vertical vorticity must develop near the surface, where it can then be intensified through convergence and vertical stretching (Davies-Jones et al. 2001). In contrast to the midlevel mesocyclone, here downdrafts play a crucial role in the formation of the low-level mesocyclone (LLM). The LLM initially develops through baroclinic generation of vorticity, primarily along the forward flank gust front, where the temperature gradient tends to be strongest. However, since the vorticity is advected upward by the low-level updraft, a strong downdraft is needed to

transport vorticity back toward the surface (Markowski et al. 2003). The rear flank downdraft (RFD) is thought to be the prime mechanism involved in the downward transport of vertical vorticity, as the vertical velocity of the RFD tends to be about one order of magnitude greater compared to the forward flank downdraft (FFD; Markowski and Richardson 2009). Furthermore, Davies-Jones (2008) presents evidence that rain curtains along the edge of the updraft and rear flank downdraft transport air with high angular momentum toward the surface and wraps inward around the low-level mesocyclone, which concentrates existing vertical vorticity near the surface.

The orientation and strength of the surface cold pool associated with the RFD can have a profound impact on the ability of warm, moist inflow to access the mesocyclone. Brooks et al. (1993) noted that, if the cold pool is too strong, the gust

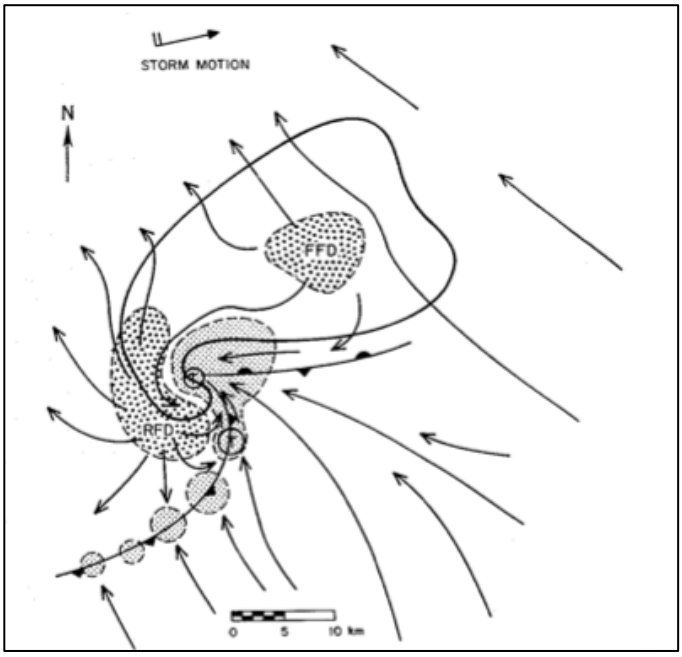

Figure 6. Schematic of near-surface tornadic supercell structure. Horizontal wind vectors are indicated by the black arrows, the forward flank downdraft (FFD) and rear flank downdraft (RFD) are coarsely stippled, the main updraft and upward motion along the rear flank gust front are finely stippled, and the radar echo is encompassed by the black contour. (From Lemon and Doswell 1979 and Davies-Jones 1985.)

front can advance too far away from the updraft. Since the gust front is needed to lift the high-buoyancy air from near the ground into the updraft, a strong cold pool can cut off the source of the buoyant air and lead to storm demise. At the same time, the cold pool appears to be an important contributor to low-level rotation, as it can enhance convergence beneath the updraft (Davies-Jones 1982).

The thermodynamic characteristics of the RFD must be considered because air from the RFD is ingested into the tornado (Davies-Jones and Brooks 1993; Wicker and Wilhelmson 1995; Adlerman et al. 1999). Markowski et al. (2002) concluded that higher-θ_e RFDs were more conducive to tornadogenesis based on observations from the VORTEX field experiment. However, Naylor and Gilmore (2014) found that the opposite was true in high-resolution simulations of a subset of tornadic and nontornadic supercells from the Thompson et al. (2003) dataset. Notwithstanding this disagreement, the importance of the behavior of the RFD is generally recognized.

2.1.3 Convective Parameters

The suitability of a convective environment for the development of tornadic supercells can be estimated through parameters calculated from a vertical profile of the atmosphere, as illustrated in Figure 3. The lifting condensation level (LCL) represents the height at which a lifted parcel becomes saturated and condensation occurs, while the level of free convection (LFC) is the level to which a parcel must be raised in order to become warmer than the environment (i.e., positively buoyant). An environment with a lower LCL and LFC for near-surface parcels requires less lift for latent heat to be

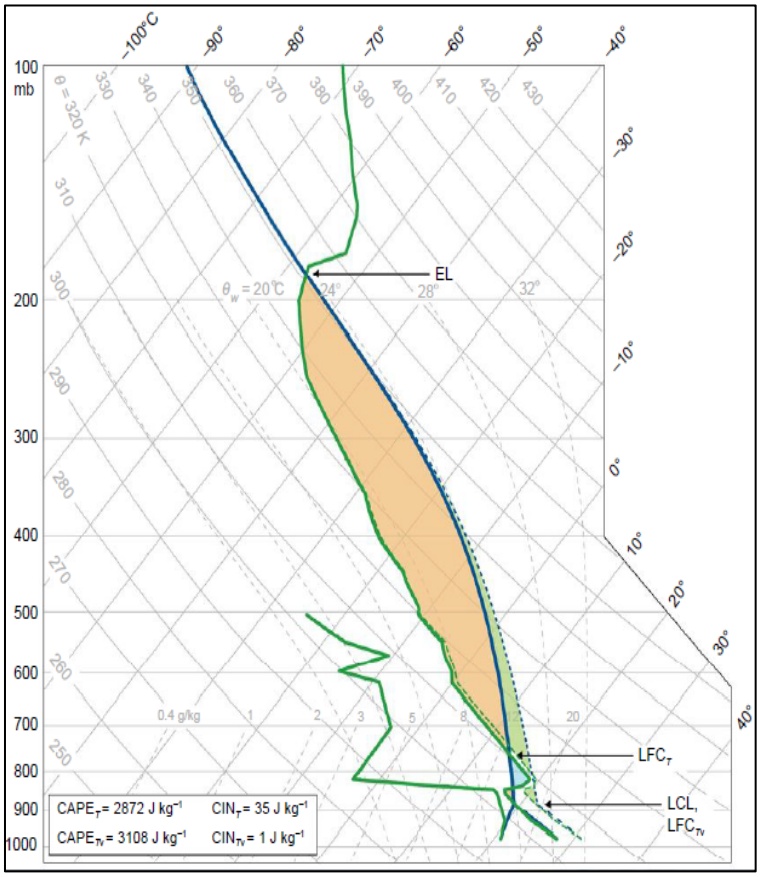

Figure 7. Skew T/ log P diagram from Del Rio, TX at 1800 UTC 14 May 2008. The lifted condensation level (LCL), level of free convection calculated with temperature (LFC_T) and virtual temperature (LFC_{Tv}), and equilibrium level (EL) are labeled with arrows. Regions of CAPE and CIN are shaded in light orange and light blue, respectively. (From Markowski and Richardson 2010, Fig. 2.9)

released and thus can facilitate storm development and organization, particularly in the lower levels (Markowski and Richardson 2010, p. 33).

The degree to which the thermodynamic profile of the atmosphere may contribute to convection is quantified by the convective available potential energy (CAPE). CAPE is the integrated positive buoyancy (B) between the LFC and the equilibrium level (EL), given by

$$CAPE = \int_{LFC}^{EL} B \, dz.$$

Buoyancy can be described by

$$B = -\frac{g}{T'}(\Gamma - \gamma)z,$$

where g is the acceleration due to gravity, T' is the environmental temperature, Γ is the parcel lapse rate, γ is the environmental lapse rate, and z is the height (Doswell 2001). By this equation, buoyancy is greater when the environmental lapse rate is steeper or when the parcel lapse rate is shallower due to latent heat release. In contrast to CAPE, convective inhibition (CIN) measures the negative buoyancy acting against a rising air parcel before it reaches the LFC and is given by

$$CIN = -\int_0^{LFC} B\, dz.$$

Environments with higher CAPE and lower CIN tend to be more conducive to supercell development (Thompson et al. 2012), and larger CAPE is often associated with significant tornadic supercells (Rasmussen and Blanchard 1998).

Storm relative helicity (SRH) measures the alignment between the storm-relative wind and the shear vector (i.e., the amount of horizontal streamwise vorticity; c.f. Figure 1) within the lower levels. This indicates the propensity for helical flow about the updraft once the horizontal vorticity is tilted into the vertical (Davies-Jones et al. 1990). SRH is given by

$$\text{SRH} = -\int_0^h \mathbf{k} \cdot (\mathbf{V} - \mathbf{c}) \times \frac{\partial \mathbf{V}}{\partial z},$$

where **V** is the horizontal velocity and **c** is the storm motion vector, integrated over a height h, which is commonly set to either 1 km or 3 km. While 0-3 km SRH is a good predictor of supercell versus non-supercell environments, 0-1 km SRH is a better discriminator of tornado potential (Rasmussen 2003).

2.2 Role of Parameterizations in Numerical Modeling of Supercells

In addition to the factors described above, processes that cannot be resolved on the computational grids of numerical models also profoundly influence simulated supercell evolution. For instance, the growth and decay of subgrid scale turbulence must be estimated using a turbulence closure scheme. By using Reynolds averaging, the Navier-Stokes equations are partitioned into mean and turbulent components (Deardorff 1980). Through analysis of squall lines simulated at horizontal resolutions ranging from 125 m to 1 km, Bryan et al. (2003) suggested that it is necessary to employ horizontal grid spacing on the order of 100 m in order to properly activate the turbulence processes associated with deep moist convection within the typical large eddy simulation (LES) regime. For supercells, Adlerman and Droegemeier (2002) used a set of simulations with horizontal resolution varying between 105 m and 2 km to demonstrate that the choice of grid spacing (and therefore the amount of unresolved turbulence) can have a profound impact on the depiction of buoyancy and velocity gradients that in turn affect the timing and frequency of cyclic mesocyclogenesis.

Likewise, water phase changes crucial to the energy budget associated with supercell development cannot be resolved explicitly in the model and must be represented through microphysical parameterizations. Such parameterizations are accomplished by assuming a size distribution for a given hydrometeor species of the form

$$N(D) = N_0 D^{\alpha} e^{-\lambda D},$$

where N is the number of hydrometeors of diameter D, and N_0, λ, and α are the intercept, slope, and shape parameters of the size distribution (Dawson et al. 2010). In a

single-moment scheme only one of the variables (e.g., λ) is allowed to vary, whereas a multimoment scheme allows the parameters to vary independently from one another.

Early supercell simulations tended to overestimate the strength and extent of the cold pool (Markowski et al. 2002), at least partially due to a surfeit of melting and evaporation of hydrometeors stemming from the use of a single-moment microphysics scheme. Dawson et al. (2007) compared the response of a high resolution simulation of the 3 May 1999 tornadic supercell to the number of moments associated with the microphysics (MP) scheme, finding that use of the multimoment schemes resulted in weaker, moister cold pools and a more realistic extent of the forward flank downdraft, which agrees more closely with field observations. Similarly, Yussouf et al. (2013) found that members of an ensemble forecast of 8 May 2003 Oklahoma City tornadic supercell that used partially and fully dual-moment microphysics had a distribution of reflectivity in the forward flank of the storm that was more similar to radar observations compared to single-moment MP members. A sensitivity study contained within Dawson et al. (2012) indicated a direct impact on the position of the mesocyclone track produced by an idealized simulation of the Greensburg, KS supercell depending on the microphysics used. The dual-moment Ziegler Variable Density (ZVD) scheme produced a forecast that more closely resembled the observed storm compared to the results from the single-moment Lin, Farley, and Orville scheme (LFO; Lin et al. 1983; Gilmore et al. 2004).

Friction is another possible source of horizontal vorticity for the tornado, although its importance relative to other processes is unclear. Many well-known idealized supercell simulations (e.g., Klemp and Wilhelmson 1978a,b; Wilhelmson and

Klemp 1978; Klemp and Rotunno 1983; Rotunno and Klemp 1985) neglect friction along the lower boundary of the domain. Tornado-like vortices have been produced in the absence of friction (e.g., Wicker and Wilhelmson 1995); however, the results of recent experiments have indicated that including friction may be necessary for the development of tornado-like vortices. In their investigation of tornadogenesis within a numerical simulation of a mesoscale convective system event, Schenkman et al. (2012) discovered interdependence between a tornado-like vortex and a strong, friction-induced rotor within the storm inflow that developed in the simulation, neither of which appeared when the model was rerun with a free slip lower boundary. Horizontal vorticity generated by surface drag and tilted upward was again demonstrated to be important for tornadogenesis in a high resolution Advanced Regional Prediction System (ARPS) model simulation of the 8 May 2003 Oklahoma City supercell (Schenkman et al. 2014).

2.3 Predictability and Error Growth in Numerical Models

Predictability can be considered in two different ways. The first is intrinsic predictability, which assumes that even with a perfect numerical model, small errors in the initial conditions will compound over time, leading to a limit on the predictability of an atmospheric feature (Lorenz 1965; 1969; 1982). The predictability is further limited by the effects from finite grid resolution, in which the unrepresented scales of motion accelerate the growth of initially small errors (Lorenz 1969). While these subgrid processes can be parameterized with some fidelity, it is impossible to fully account for all scales of motion. Lorenz (1982) observed that the length of time over which

numerical errors double decreases with the scale of a feature, meaning that such error growth on the storm scale may be on the order of one hour to minutes, especially for a more localized feature such as a low-level mesocyclone in a supercell thunderstorm.

In the realm of operational forecasting, it is most relevant to consider practical predictability, which is limited by errors in the initial conditions and model formulation that could theoretically be avoided and are therefore more realistic (Lorenz 1996; Zhang et al. 2006; Baxter 2011). Sources of these types of errors include the spatial density of observing networks, instruments themselves, deficits in model parameterization schemes, and grid resolution. (For example, when modeling mesoscale convective systems, Baxter (2011) found that smaller scale errors propagated to broader scales more rapidly when using finer grid resolution.) Using an ensemble-based approach to numerical weather prediction can help to mitigate some of this uncertainty by considering the overall effect of changes to the initial conditions (Brooks et al. 1992).

It should be noted that, although the focus tends to be on upscale propagation of errors on smaller scales, Durran and Gingrich (2014) recently called attention to the nearly equal importance of downscale error propagation from the mesoscale. This idea is supported by a predictability study of a Pacific Northwest snowstorm by Durran et al. (2013), in which large-scale perturbations to the synoptic environment grew more rapidly within a 12 hour time period and had more influence on the discrimination of "rain-likely" vs. "snow-likely" ensemble members than perturbations at smaller scales did. Similar results were obtained in a study of flow over complex terrain by Reinecke and Durran (2009) and a heavy precipitation event by Bei and Zhang (2007). Therefore,

it seems reasonable to consider such error sources when studying the predictability of storm-scale features associated with supercells.

The Warn-on-Forecast initiative seeks to predict hazards such as tornadoes with sufficient accuracy to issue a warning with 30-60 min of lead-time (Stensrud et al. 2009). This approach assesses probability over time and space based on the forecast solutions of multiple ensemble members. Given the impossibility of measuring the storm environment perfectly, the increased rate of error growth as scale decreases, and the importance of storm-scale features to the formation of low-level rotation and tornadogenesis in supercells, it is important to consider the relative impact of environmental errors on supercell dynamics that may affect the forecast.

Cintineo and Stensrud (2013) investigated a possible upper limit of predictability for supercell thunderstorms by examining the effects of varying degrees of perturbations to a control atmospheric profile. A database was created from observed 1-, 2-, and 3-hour forecast errors in the 13 km Rapid Update Cycle (RUC) model on 70 days in 2011 that were favorable for supercell development. Perturbations to the wind, temperature, and humidity profiles were randomly selected from this database and applied at prescribed levels to create three 100-member ensembles of storm environments, one for each forecast lead time. Each storm simulation was run with horizontally homogeneous initial conditions at 1 km horizontal resolution for a total of three hours. As anticipated from error growth theory, the magnitude of the RMSE for these variables increases with a longer forecast period (Figure 4). This study seeks to extend the work of Cintineo and Stensrud (2013) by examining the sensitivity of low-level, submesocyclone-scale vortices to small perturbations in the storm environment

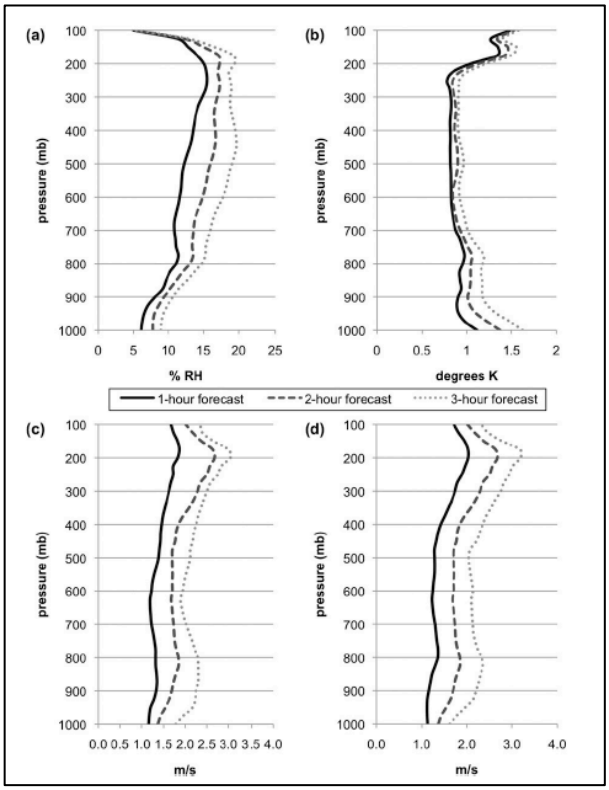

Figure 8. Root mean square errors (RMSE) of the (a) relative humidity, (b) temperature, and (c) u- and (d) v-components of the wind for 13 km RUC errors at forecast time of 1 hr (bold), 2 hr (dashed), and 3 hr (dotted). (From Cintineo and Stensrud 2013.)

using large-eddy simulations of tornadic supercells. Following Bryan et al. (2003), a large-eddy approach should help reduce uncertainties from the sub-grid turbulence scheme and permit a more accurate evaluation of the predictability of mesocyclones and submesocyclone-scale features as a function of the background mesoscale environment and its known error structure.

Chapter 3: Methodology

3.1 Model Configuration

The supercell thunderstorm simulations were generated using CM1, a three-dimensional, nonhydrostatic atmospheric model suitable for convection at large eddy simulation (LES) resolutions (Bryan and Fritsch 2002). CM1 is highly scalable and runs very efficiently, which is advantageous for the high resolutions and large number of simulations required for this project. The model includes a variety of microphysics and turbulence parameterizations that are relevant to convective modeling without being complicated by the additional numerical weather prediction capabilities, such as radiation and grid nesting, that are included in models such as Weather Research and Forecasting (WRF) and ARPS but are unnecessary for this application. The simulations were run on the University of Tennessee's Kraken supercomputer at the National Institute for Computational Sciences (NICS) with 7500 cores for approximately 6.5 hours each.

A summary of the model settings used for the simulations is listed in Table 1 (the text of the complete CM1 namelist file is included in Appendix A). In order to adequately resolve low-level vortices in the storm, a uniform horizontal grid resolution of 100 m was used. Although tornado-like vortices would be better resolved at higher resolutions, initial experiments conducted at $\Delta x = 50$ m revealed potential stability issues near the surface that could negatively impact the behavior of low-level vortices that may develop in the simulation. Additionally, the reduced computational expense at $\Delta x = 100$ m allowed a greater number of simulations to be run and increased the speed of post-processing the data. The vertical grid was stretched geometrically with Δz

Table 1. Summary of CM1 model parameters used for all simulations.

Parameter	**Setting**
Horizontal grid spacing	100 m
Vertical grid spacing	40 m ≤ Δz ≤ 500 m
Large integration time step	0.5 s
Grid stretching function	Geometric
Small integration time step	0.083 s
Grid motion vector (*u*, *v)*	(8 m s^{-1}, 6 m s^{-1})
Thermal perturbation	
Magnitude	3.0 K
Horizontal Radius	10.0 km
Vertical Radius	1.5 km
Height of Center (AGL)	1.5 km
Surface drag coefficient	0.0104
Microphysics	3-moment ZVD
Boundary conditions	
Top	Rigid with Rayleigh damping layer
Lateral	Open-radiative
Turbulence	Isotropic 1.5-order TKE

ranging from 40 m at the surface to 500 m at the top of the domain. This conserved vertical grid points by maximizing the vertical resolution in the lowest levels of the storm, the area of primary interest in this study. The 3D grid consisted of 1200 x 1200 x 106 points, for a total spatial extent of 120 km x 120 km x 21.5 km. Horizontal grid points were conserved by translating the grid at a motion vector of (8 m s^{-1}, 6 m s^{-1}), which was the estimated storm motion derived from the control sounding. This setting was used for all of the simulations, since the storm motion with the perturbed soundings was not expected to deviate drastically from the control.

The goal of the simulations was to isolate the effect of perturbations to the initial environment by simplifying the conditions imposed on the model, while, at the same time, making those conditions as realistic as was reasonable. The domain was initialized with one of the perturbed soundings (described in further detail below) to create a horizontally homogeneous storm environment. Convection initiation was induced with a 3 K thermal bubble with a vertical and horizontal radius of 1.5 km and 10 km, respectively, centered at 1.5 km AGL.

Friction was enabled along the lower boundary of the domain to better reflect an actual storm environment. Many of the well-known numerical simulations of supercells (e.g., Weisman and Klemp 1982; Wicker and Wilhelmson 1995) neglect the effects of friction along the lower boundary, but there is also evidence that use of drag may be helpful for tornadogenesis (Schenkman et al. 2012; Schenkman et al. 2014). The turbulence mixing length of the lower boundary was set to 10 cm, which was selected after comparing the results of test simulations with 5 cm, 10 cm, and 20 cm mixing lengths. Computational expense increased with greater mixing length, so 10 cm was selected as a compromise. Turbulence was assumed to be isotropic since $\Delta x \sim \Delta z$ near the surface and was parameterized with a 1.5-order closure, Deardorff-based turbulence kinetic energy (TKE) scheme (Deardorff 1980; Stevens et al. 1999).

The accuracy of the microphysics scheme employed in atmospheric models can have a profound impact on the evolution of supercells, especially in the characteristics of the cold pool. A three-moment formulation of the Ziegler Variable Density (ZVD) scheme was employed for these simulations as a best effort at capturing the interactions

of ice species in the cloud that in turn affect the thermodynamic processes within the storm. (Mansell and Ziegler 2013; Dawson et al. 2014).

3.2 Sounding Perturbations

The sets of perturbed soundings were generated after the method employed by Cintineo and Stensrud (2013). Using archives of 13 km RUC model runs over the CONUS, they developed a set of typical errors for 1-, 2-, and 3-hour forecasts of the environmental profile on 70 days during which atmospheric conditions were favorable for supercell development. Errors from this dataset were randomly selected and applied to u, v, q_v, and θ at the pressure heights given in Table 2. The vertical profile between these points was interpolated using a polynomial spline, after which the perturbation profile was added to a control sounding to construct the final perturbed sounding.

For the present investigation, an environmental sounding observed near Geary, Oklahoma, on May 29, 2004, the day of a significant tornadic supercell, served as the

Table 2. Pressure heights (hPa) at which randomly selected RUC errors were inserted into the control sounding. (From Cintineo and Stensrud 2013.)

RH	Temperature	*u*	*v*
100	100	100	100
300	200	200	200
500	400	400	400
700	600	600	600
800	800	800	800
900	900	1000	1000
1000	1000		

control. Errors from the 1-hour forecasts were scaled to 10%, 25%, and 50% of their original magnitude and then randomly applied to the control sounding to generate a total of 20 different perturbed soundings for each magnitude of model errors. The control sounding was also used to run a simulation and was included as a member in all three ensembles.

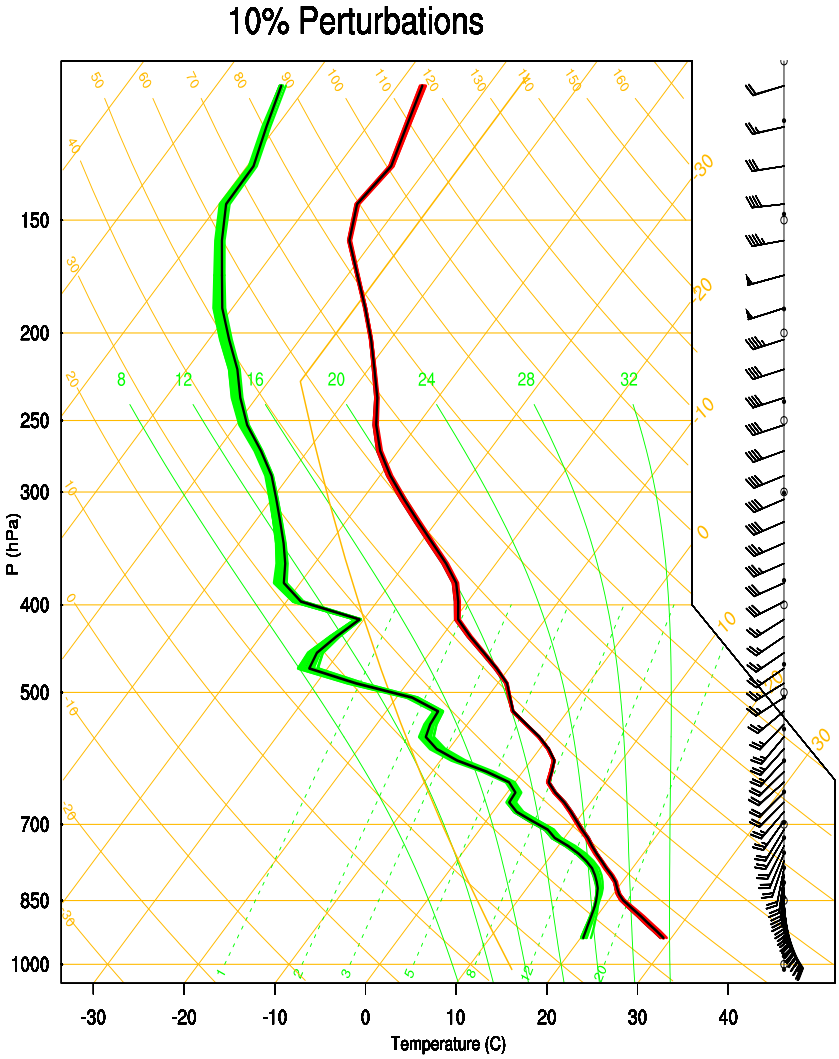

Figure 5. Overlay of all soundings perturbed with randomly selected RUC errors scaled to 10% of the original magnitude with the control sounding denoted in black.

Figures 5-7 contain composites of the soundings from each of the three ensembles. The overlaid black line denotes the control sounding from which the perturbations originated for comparison. Throughout most of the depth of the column, the control profile falls near the middle of the perturbations in each group. There does, however, appear to be a dry bias in the perturbations from 400-150 hPa, particularly in

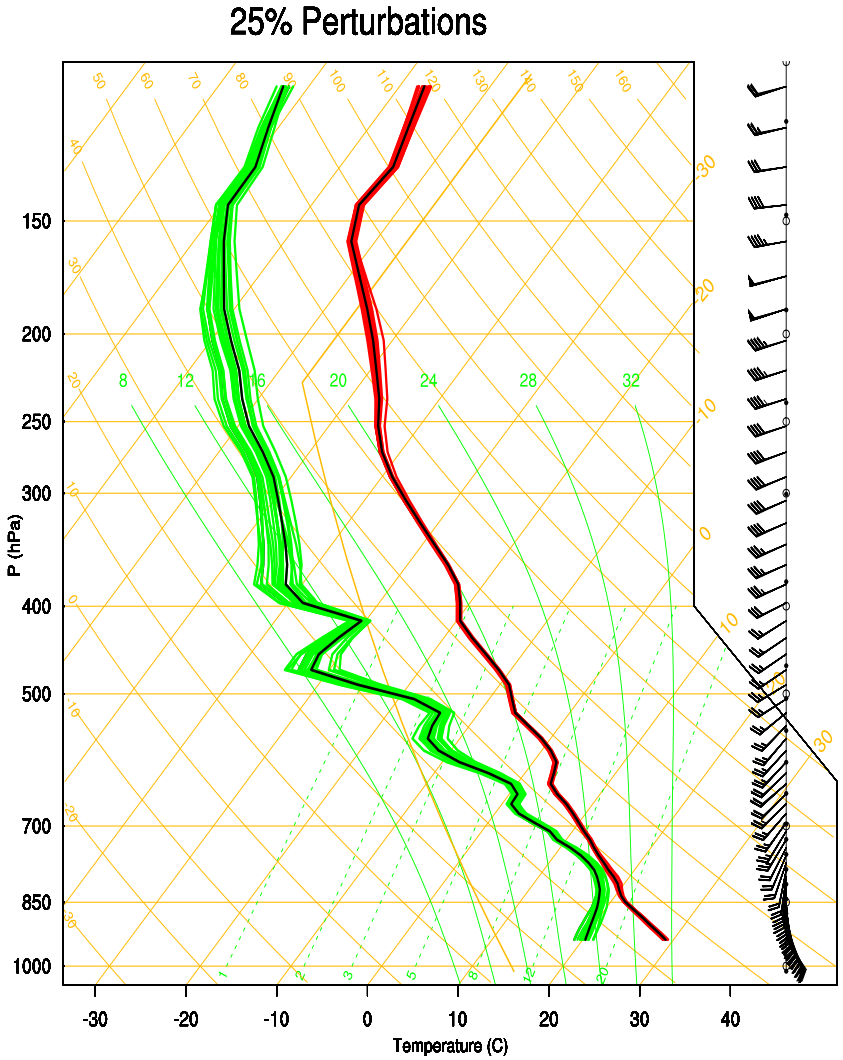

Figure 6. Overlay of all soundings perturbed with randomly selected RUC errors scaled to 25% of the original magnitude with the control sounding denoted in black.

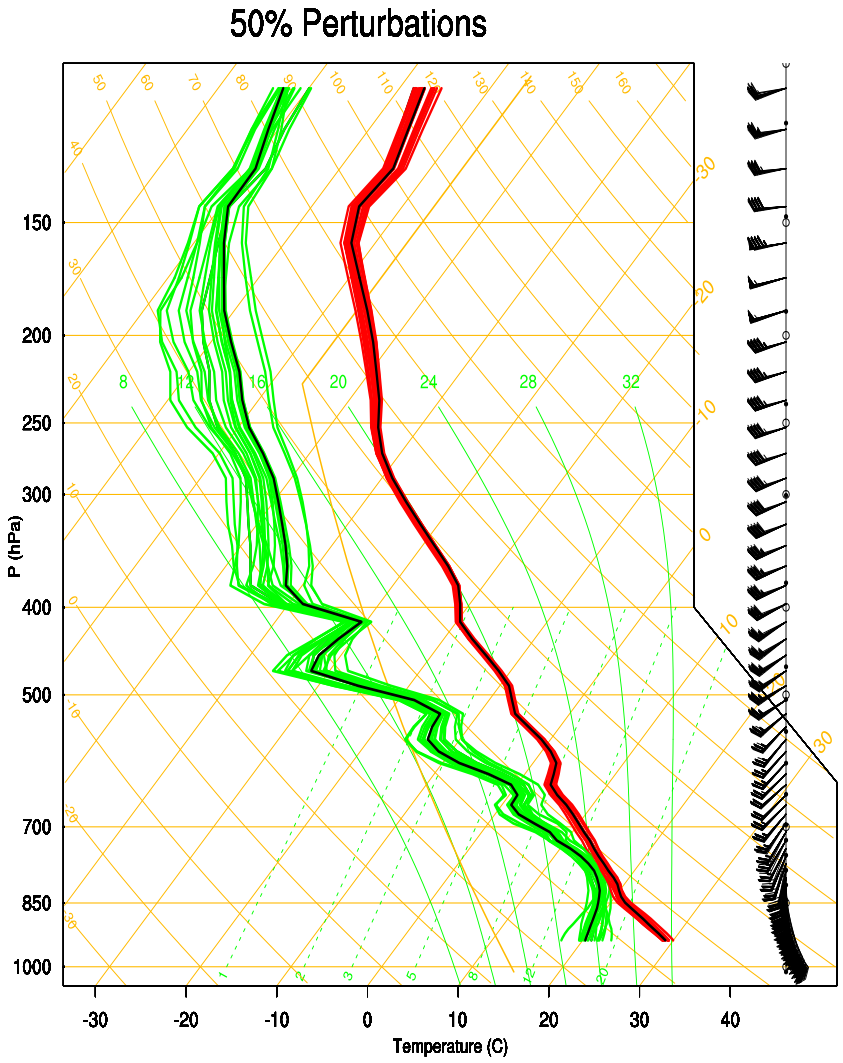

Figure 7. Overlay of all soundings perturbed with randomly selected RUC errors scaled to 50% of the original magnitude with the control sounding denoted in black.

the 10% and 50% ensembles, with an additional moist bias below 750 hPa just in the 10% ensemble. In the 50% ensemble, there appears to be a slight cool bias between 400 hPa and 175 hPa.

Overlays of the 0-6 km AGL hodographs from each ensemble including a black line to denote the control sounding are plotted in Figure 8, with the 10%, 25%, and 50%

ensembles, respectively, moving clockwise from the top left corner. The 10% and 25% ensemble hodographs have no discernable difference in shape, and the wind speed only varies by about 1 m s^{-1} across the ensemble for each. A more noticeable variation occurs in the 50% ensemble. In the lowest 1 km of the sounding, the wind speed of one

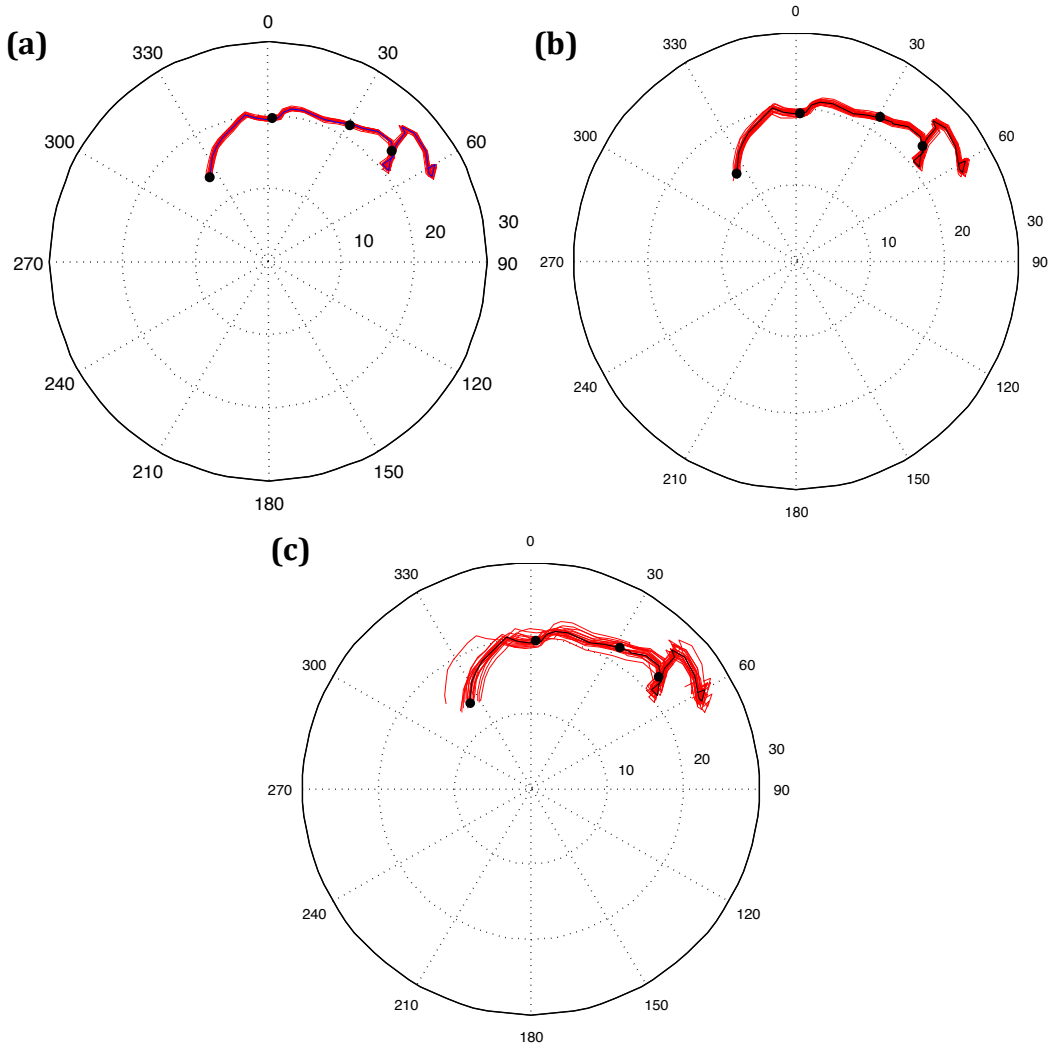

Figure 8. Composites of hodographs from the 10% (a), 25% (b), and 50% (c) error ensembles. Black dots indicate surface, 1 km, 2 km, and 3 km AGL heights, ascending from left to right.

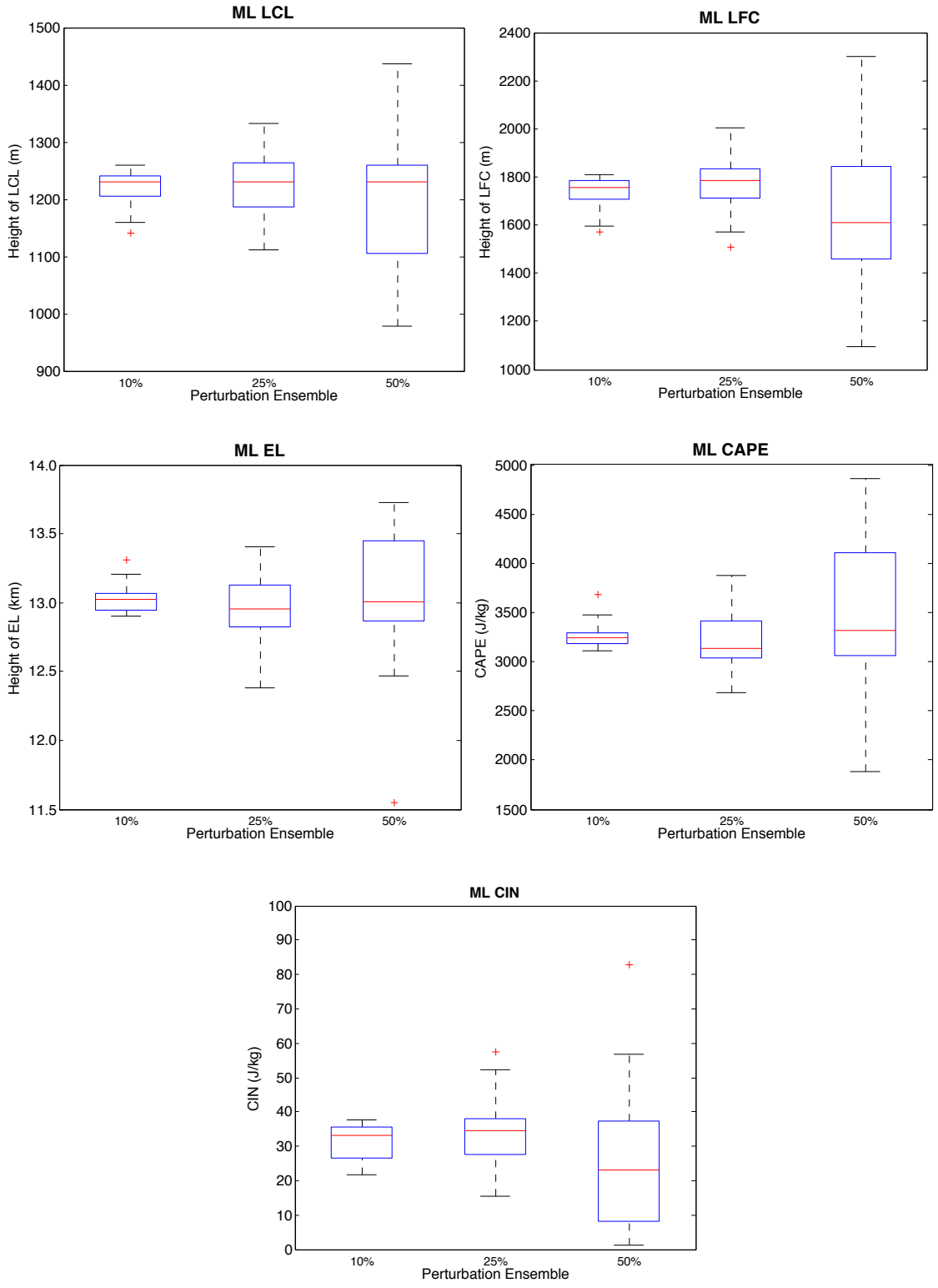

Figure 9. Box-and-whiskers plots of the spread in mixed layer LCL, LFC, EL, CAPE, and CIN for the 10%, 25% and 50% error ensembles.

ensemble member differs from the others by about 3 m s^{-1}. The overall spread in wind speed for all members is close to 3 m s^{-1} throughout the depth of the hodograph, although the spread is a bit larger than this near the surface. While the 10% and 25% ensembles did not contain any changes in the shape of the hodograph, the 50% ensemble contains several members that deviate from the control, particularly near 1 km AGL.

Convective parameters were calculated for each of the soundings to assess how the environments were affected by the perturbations. The statistics for each of the ensembles are summarized in the box plot in Figure 9. As the magnitude of the perturbations increases, the standard deviation and range of each of the parameters also increases nearly commensurately. The medians of the parameters vary without any discernable pattern. Since the perturbations are randomly selected, it is possible for the center of the data to be skewed slightly higher or lower. While not ideal, this is less important than seeing a coherent change in the standard deviation with perturbation magnitude.

3.3 Vortex Detection and Classification (VDAC) algorithm

In order to identify low-level vortices within the storms, the Vortex Detection and Classification (VDAC) algorithm described in Potvin (2013) was used to analyze the wind field from the supercell simulations. VDAC applies a model of a modified combined Rankine vortex (MCRV) embedded within a background flow that is a combination of spatially constant, linearly sheared, and linearly divergent in character, which is represented by

$$u = \mathrm{a} + \mathrm{by} + \mathrm{cx} + \mathrm{V}_R\mathrm{R}(\mathrm{x} - \mathrm{x}_0) - \mathrm{V}_T\mathrm{R}(\mathrm{y} - \mathrm{y}_0), \qquad \mathrm{r} < \mathrm{R},$$

$$= a + by + cx + R_\beta V_R(x - x_0)r_\beta + 1 - R_\alpha V_T(y - y_0)r_\alpha + 1, \quad r \geq R,$$

$$v = d + ex + fy + V_R R(y - y_0) + V_T R(x - x_0), \qquad r < R,$$

$$= d + ex + fy + R_\beta V_R(y - y_0)r_\beta + 1 + R_\alpha V_T(x - x_0)r_\alpha + 1, \quad r \geq R,$$

where

$$r = (x - x_0)^2 + (y - y_0)^2,$$

a and d are the x and y components of the uniform flow velocity (m s^{-1}); b and e are the components of the horizontal shear (s^{-1}); c and f are the components of the horizontal divergence (s^{-1}); (x_0, y_0) are the vortex center coordinates (m); R is the vortex radius of maximum wind (m); V_T and V_R are the maximum tangential and radial vortex velocities (m s^{-1}), respectively; and α and β are the radial decay exponents for the vortex tangential and radial winds, respectively (Potvin 2013).

Analysis domains are selected by first dividing the full domain of the input wind at a given level and time step into 6 km square regions and identifying which contain at least one grid point at which the vertical vorticity ζ is greater than 0.01 s^{-1}. Regions that meet the criteria are then divided into 25 points, which are the centers for additional 6 km x 6 km analysis subdomains. These points serve as first guesses of the vortex location.

The VDAC algorithm progresses through a series of steps to fit its numerical model equations to the input wind field within each subdomain and extract any vortices that are present, illustrated with output from one of the simulations in Figures 10 and 11. The process begins in Figure 10a with a 6 km x 6 km region about one of the first-guess vortex centers (top left). All coefficients relating to the vortex in the model are

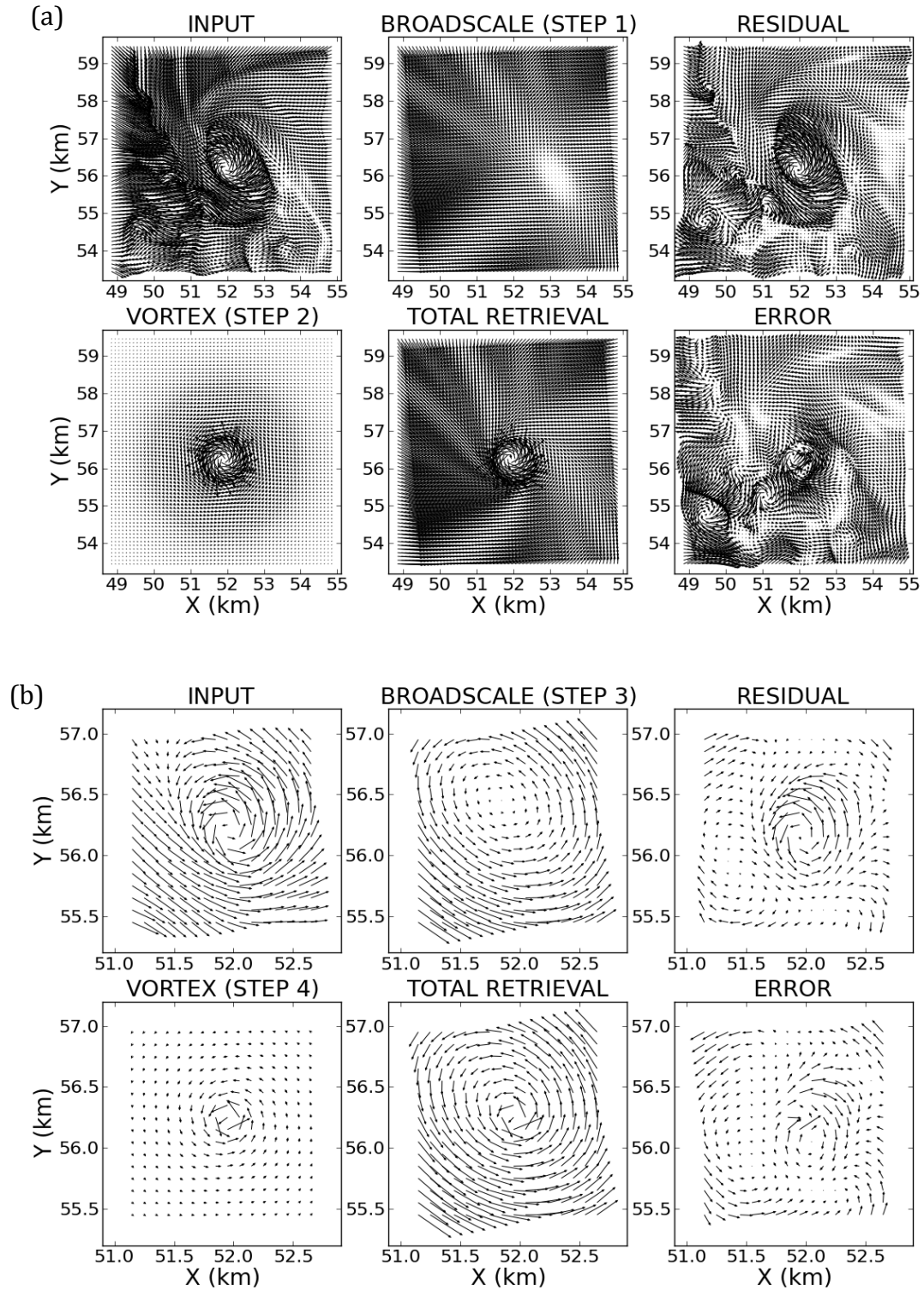

Figure 10. Example of VDAC algorithm analysis process with wind output from one of the simulations. Steps 1-2 are show in (a), and Steps 3-4 are shown in (b). (Formatted after Potvin 2013.)

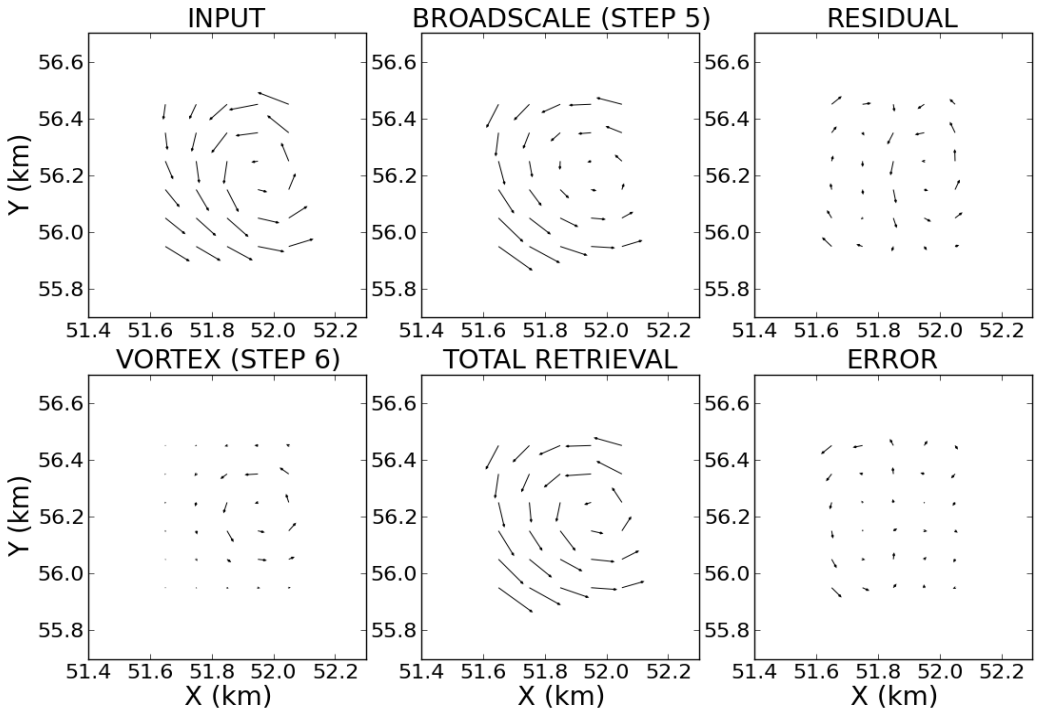

Figure 11. Continuation of VDAC analysis for a vortex meeting the minimum detection criteria after Step 4. (Formatted after Potvin 2013.)

set to zero while the background flow components are fitted to the input wind field (top center). The background-only flow is subtracted from the input (top right), which becomes the input for Step 2. Next, all vortex terms in the model equations are fitted to the residual flow (bottom left). The total retrieval is the calculated vortex superimposed on the calculated broadscale flow (bottom center). Analysis will continue if this retrieved vortex meets the minimum criteria for detection.

Steps 3 and 4 are the same as Steps 1 and 2, except the initial input is the total retrieved vortex field from the first pass with the domain centered on an area of radius 1.5*R* (Figure 10b). If this retrieval meets the criteria as well, analysis proceeds to the third and final pass. The radius is set to *R*, while the center of the domain remains at the

same location as in the second pass. The algorithm then calculates characteristic variables for the vortex, namely the location of the vortex center (x_0, y_0), R, V_T, and the circulation C at a radius of 1 km around the center.

Each detected vortex was required to have a minimum radius of 100 m (equal to the horizontal grid spacing) and tangential wind speed greater than or equal to 15 m s^{-1}. Anticyclonic vortices (those with negative V_T) were also neglected to simplify later analysis. Most low-level vortices in the northern hemisphere rotate cyclonically, and anticyclonic vortices are typically weak and brief in comparison.

As a simple test for vertical continuity, the VDAC algorithm was run at 100 m, 500 m, and 1000 m above ground level (AGL) for each simulation. Each 100 m vortex center retrieved from the wind field was required to have corresponding vortex centers at 500 m and 1000 m AGL located within 45° of a vertical line drawn through that point. Temporal continuity was not judged directly, as there were occasional gaps in the vortex detections. This could be a result of either a brief weakening of the vortex such that it no longer meets the minimum thresholds or an actual termination of the vortex event. Instead, *each individual detection was considered to be an event in time.*

Chapter 4: Results

4.1 General Storm Evolution

Reflectivity calculated from the model output at z = 1 km AGL was used to observe the general development of the storms. Storm behavior overall is similar among ensemble members and across the ensembles, although differences in storm-scale features appear during the course of the simulation, particularly with the perturbations.

From the reflectivity plots, it became apparent that some simulations were contaminated by extraneous convection to the southeast of the main storm (Figure 1). This resulted from interactions between the southern boundary and atmospheric waves in environments with large instability. As the size of the perturbations increased, the number of simulations exhibiting this behavior increased, and it occurred earlier in the

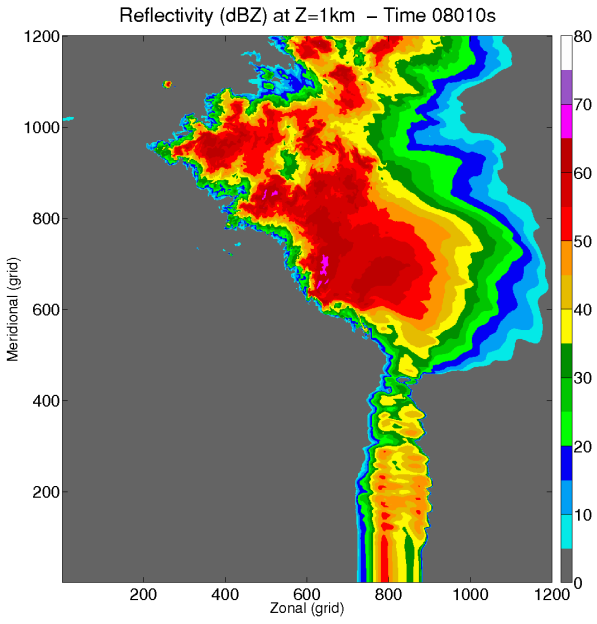

Figure 12. Example of erroneous convection induced by boundary conditions.

simulation. Once this feature appeared, it tended to affect more of the surrounding area as time continued, interfering with the right moving supercell and negatively impacting the character of the inflow. For these reasons, it was necessary to exclude the remainder the simulation from further analysis once this feature appeared.

4.1.1 Control Simulation

Selected frames of the 1 km AGL simulated reflectivity field for the control run are shown in Figure 13. The first appearance of a reflectivity signature occurs within about 1800 s of model initiation. By t = 2700 s a hook-like appendage has formed on the rear flank of the southern storm. Storm splitting occurs on multiple occasions: once at t = 3000 s, shortly after the hook echo materializes, and again at t = 4200 s. While the initial left split storm moves north and remains fully discrete, eventually splitting itself, the second left split lingers along the left flank of the parent storm and seems to increasingly interact with it during the final 1800 s of the simulation.

4.1.2 10% Perturbation Ensemble

Contours of reflectivity exceeding 30 dBZ for each model output time were overlaid to qualitatively assess the similarity of storm evolution among the members of each ensemble. In the 10% ensemble (top row, Figure 14), the contours for all simulations are well aligned and are generally located within approximately 5 km of one another during the first 3600 s of the simulation. This includes the beginning stages of the first storm split, where concurrent notches develop on the northern side of the

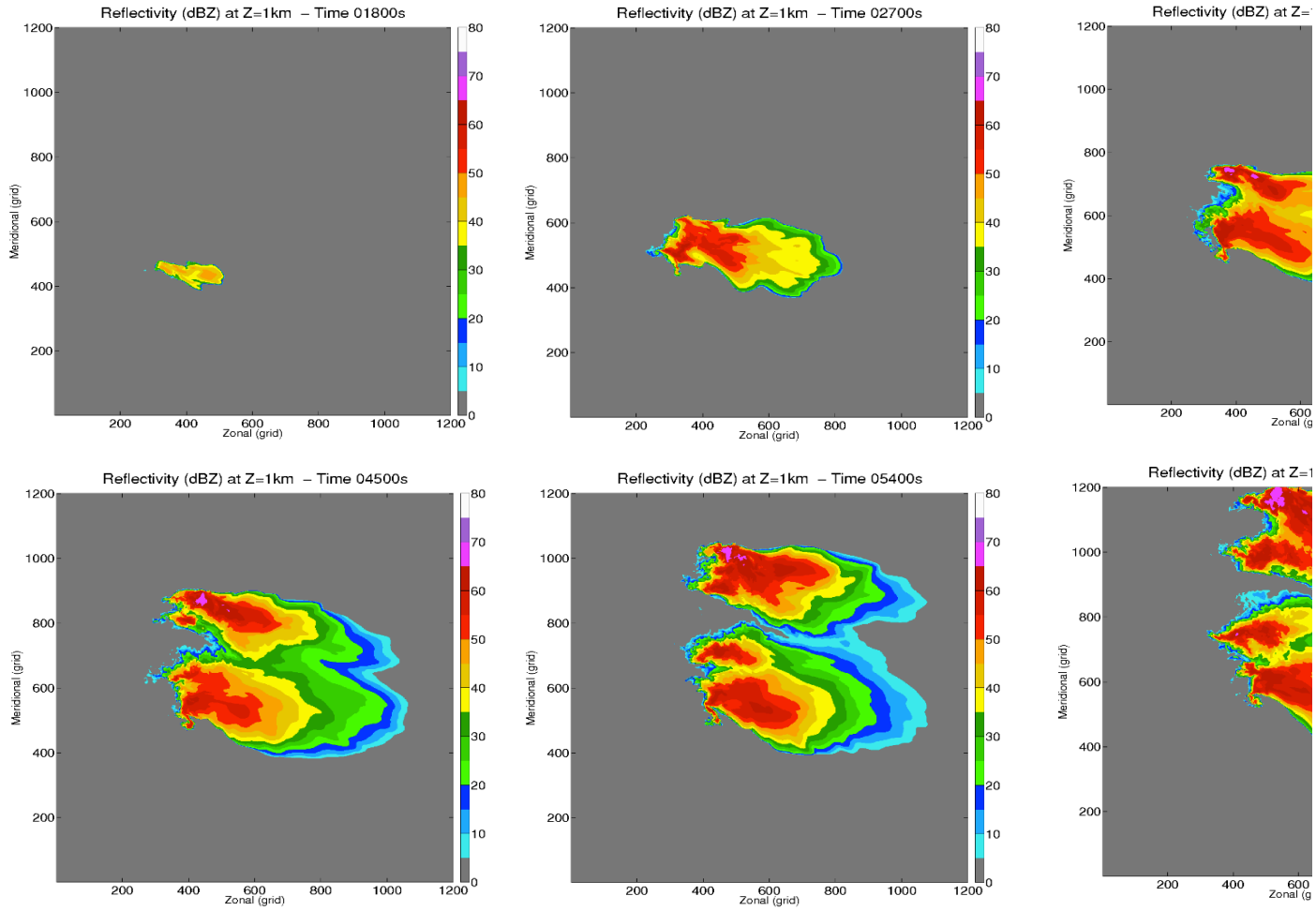

Figure 13. Simulated reflectivity (dBZ) at 1 km AGL over time in control sounding simulation.

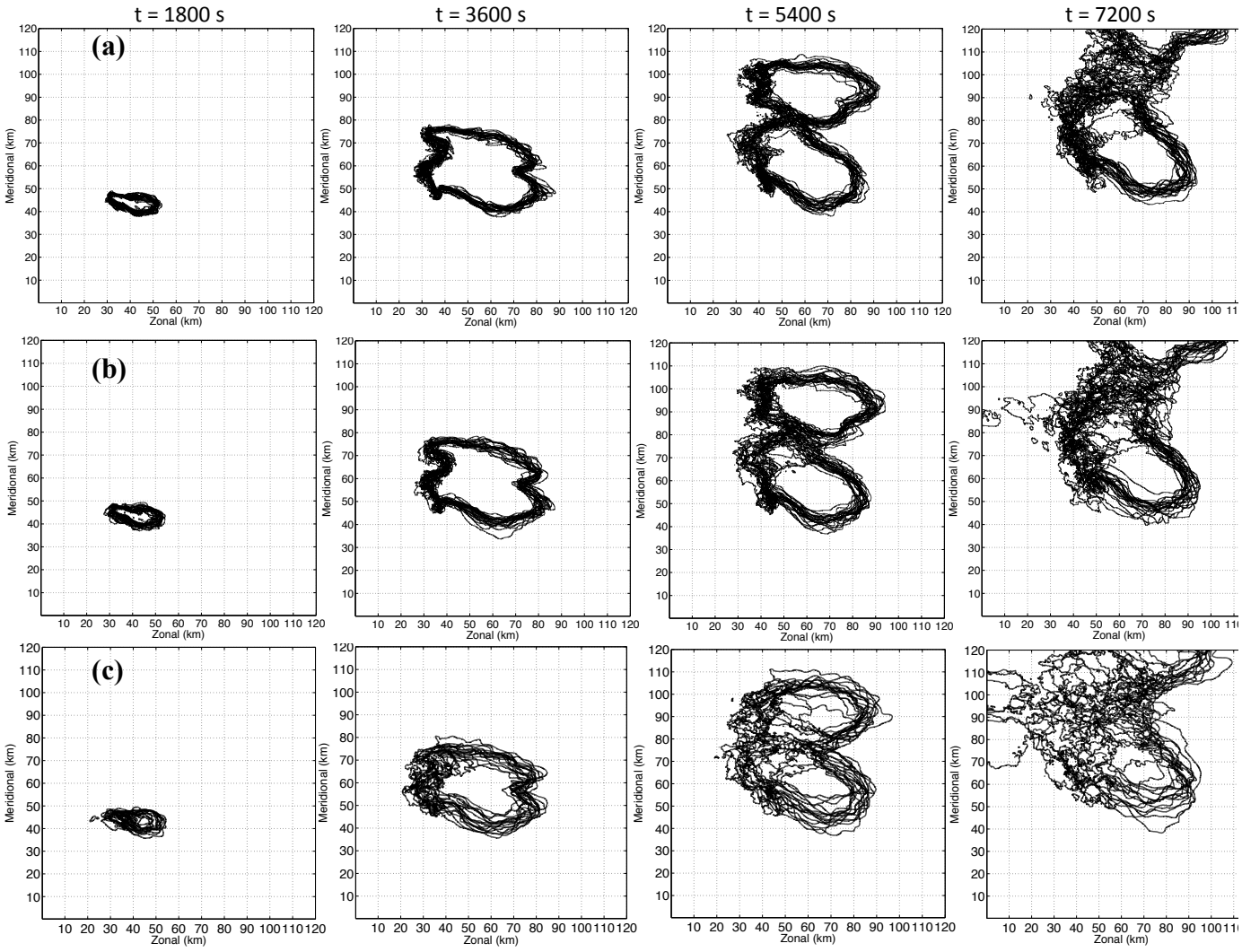

Figure 14. 30 dBZ reflectivity contour at 1 km AGL for all members of the (a) 10%, (b) 25%, and (c) 50% error ensembles.

parent supercell. All members exhibit a hook appendage along the rear flank, although the exact shape is not consistent.

Although the first instance of storm splitting that was noted in the control run occurs universally across members, the details of the timing vary noticeably. After the first hour, there is a discrepancy of several minutes with regard to when the two storms completely separate from each other. One member accomplishes this by t = 4200 s, while the rest gradually follow suit over the course of the next several minutes. This, in turn, affects the timing of the second split, and the solutions from the simulations continue to diverge from one another. Noticeable variation also occurs in the completeness of the separation between the second split and the parent storm and, if the left split fully separates, the degree of interaction between the two storms. Despite this, the location of the parent storm continues to be quite consistent among ensemble members for the duration of the analysis time.

4.1.3 25% Perturbation Ensemble

As in the 10% perturbation ensemble, the 25% perturbation ensemble members (middle row, Figure 14) agree well on the extent and location of the simulated reflectivity signature of the storm at t = 3600 s, with only about 5 km of spread in the reflectivity contours. There appears to be more disagreement in the depiction of the forward flank region of the storm, however. Unlike in the 10% ensemble, there was not a clear temporal outlier among the 25% simulations during the first storm splitting phase. During the remainder of the simulation time, the storms from each ensemble become increasingly divergent from each other in space, with the N-S position of the

forward flank of the parent supercell varying by nearly 20 km among the ensemble member by t = 6900 s. Even more disagreement occurs in the timing of the second split, if it even occurs. Some members appear to begin to split, but the left mover never totally separates from the right mover.

4.1.4 50% Perturbation Ensemble

As might be anticipated based on the greater range in the sounding parameters, the storms produced in the 50% perturbation ensemble exhibited greater variation in how rapidly they developed compared to the other ensembles (bottom row, Figure 14). The overall spread in the reflectivity contours is already 10-20 km on the east and west sides of the storm by t = 2400 s, although the spread along the northern and southern flanks is similar to what was observed at this time in the 10% and 25% ensembles. This is due to a combination of variation in the time that reflectivity signatures appear and slight differences in the storm motion. After t = 3600 s, the contour spread is 10-15 km on all sides of the storm and continues to grow as the simulation progresses. Again, the timing of the first left split varies between ensemble members and contributes to continuing divergence in the solutions.

4.2 Vortex Characteristics

4.2.1 Total Vortex Count

Column graphs of the total number of vortices detected for each member of the ensembles through t = 7200 s are shown in Figure 15. Again, each vertically continuous vortex was counted as a separate detection with no attempt to establish temporal

continuity. Pert009 in the 50% ensemble developed spurious convection after t = 6990 s, so any vortices that were detected after that time were discarded. The most noticeable difference occurs in the magnitude of the totals in the 50% ensemble, where the non-zero vortex counts are about 3 times higher than those observed in the 10% and 25% ensembles. Changing the magnitude of the errors from 10% to 25%, however, does not appear to have a considerable impact on the vortex totals.

An F-test was used to statistically compare the variances of each ensemble's vortex totals distribution to each of the others with a null hypothesis that the variances of the distributions are not statistically different from each other. The resulting p-values were 0.083 for the 10% vs. 25% test, 3.45×10^{-4} for 10% vs. 50%, and 5.89×10^{-7} for 25% vs. 50%. With a confidence of 95%, it is shown that there is a statistically significant difference in the variances between the 50% ensemble and the other two. The variances of the 10% and 25% ensembles, however, may not be statistically different from each other, since the null hypothesis could not be disproven.

As a cautionary note when interpreting the data in the 50% ensemble, data loss in the output from the atmospheric model occurred for t = 4050 – 4500 s, making it impossible to determine if vortices were present during that time span. The totals given in Figure 15, therefore, do not include that data. In spite of this, the distribution is significantly different from the other two ensembles and would possibly be even more so with the addition of any vortices that may have developed during that time frame.

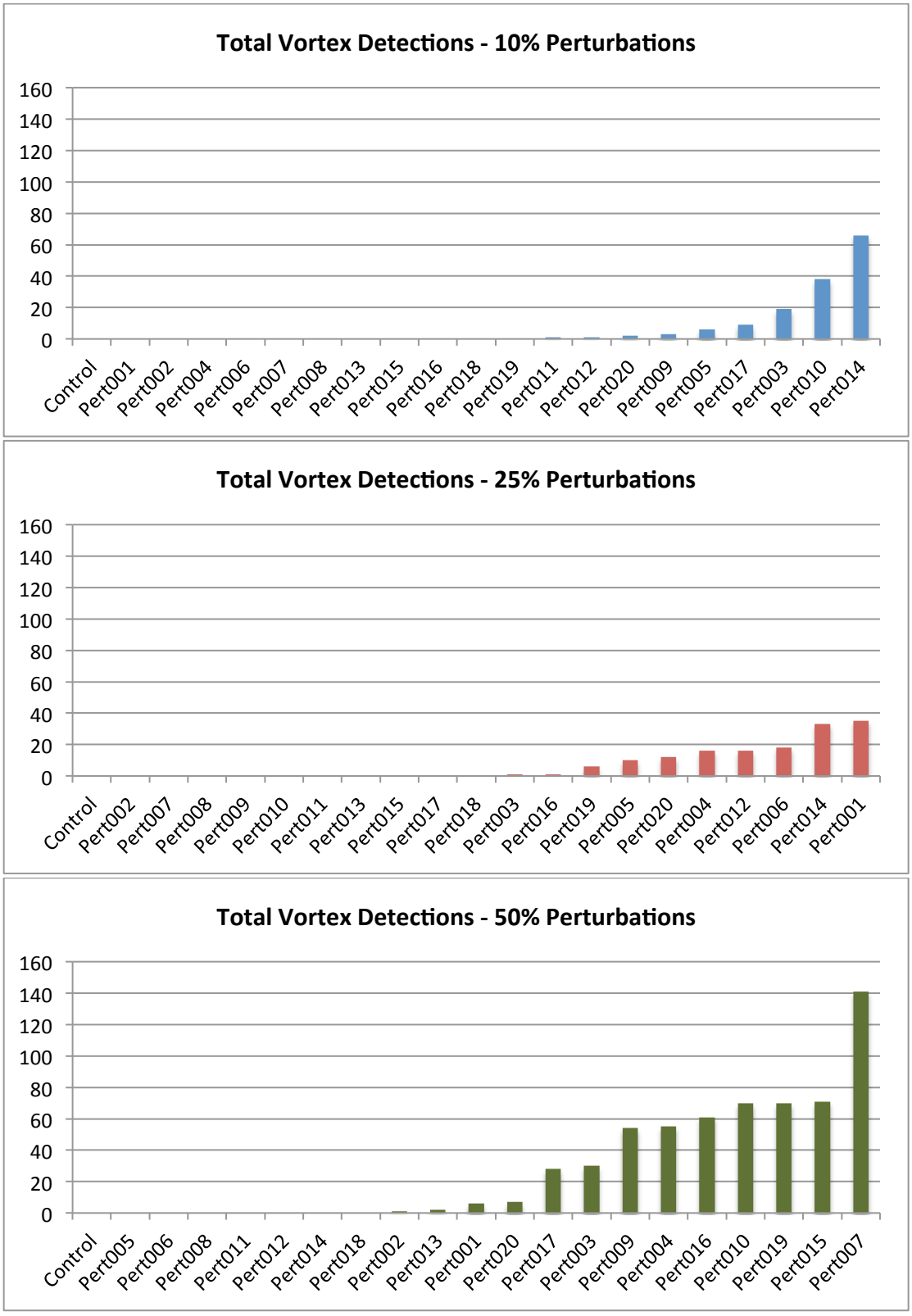

Figure 15. Total detected vortices up to t = 7200 s for the 10%, 25%, and 50% ensembles.

4.2.2 Spatial Distribution of Vortex Detections

The spatial distributions of all vortices detected with each ensemble are contained in Figure 16, where the points are colored according to the time at which the detection occurred. While Figure 15 indicates that the that the total number of vortices did not vary considerably between the 10% and 25% ensembles, the scatter plot reveals that the points are more widely scattered with the larger perturbations. This is further substantiated in the 50% ensemble plot in Figure 17, where the detections are even more dispersed and comprise longer tracks that in the smaller perturbation ensembles. The points occur at a wider range of times as the perturbation size increases, with the 50% ensemble containing many more points in the first hour of the simulation that the

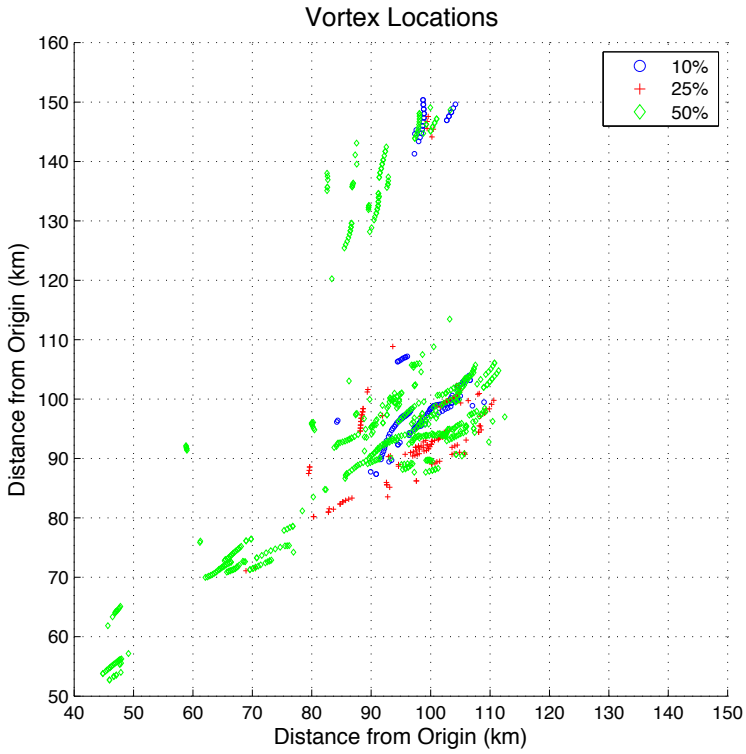

Figure 16. Overlay of vertically continuous vortex detection locations during first 7200 s of simulation time for each ensemble (10% in blue, 25% in red, and 50% in green).

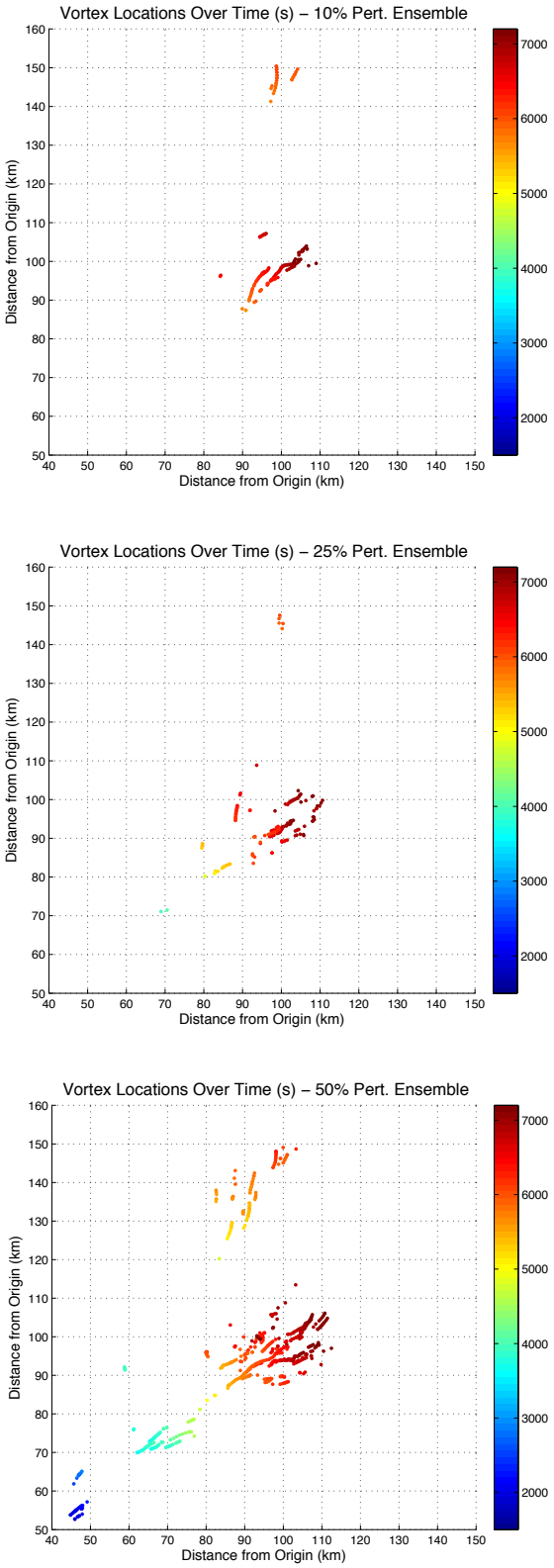

Figure 17. Vertically continuous vortex detection locations for each ensemble, colored according to time of occurrence, during first 7200 s of simulation time.

other two ensembles. It seems likely that the greater total number of vortices in the 50% ensemble was facilitated in part by the ability of the simulated storms to organize more rapidly compared to those generated from lesser perturbations.

A secondary cluster of vortices that met the vertical continuity and wind speed criteria is located to the north of the main swath. Almost all of the parent supercells in the simulations produced a left split, some of which also split to produce a cyclonically rotating supercell that produced a vortex. In other cases, additional convection developed independently to the north of the parent supercell.

Two gaps are present in the spatial distribution for the 50% ensemble. The later gap coincides with the period of data loss during t = 4050 – 4500 s. The first gap, however, occurs naturally in the data for three of the ensemble members, although the cause is unclear.

4.2.3 Time of First Detected Vortex

The time of the first detected vortex that met the vertical continuity and strength criteria during the entire three-hour simulation is plotted in Figure 18. Pert005 in the 50% ensemble produced its first vortex after the domain had already become contaminated by the boundary condition convection and is therefore left blank in the chart. Pert008 in the 10% ensemble and Pert006, Pert014, and Pert018 in the 50% ensemble were also left blank because they never produced vortices during the three hours of simulation time. It is unclear whether or not vortices may have developed eventually in those ensemble members if the simulation had run beyond three hours.

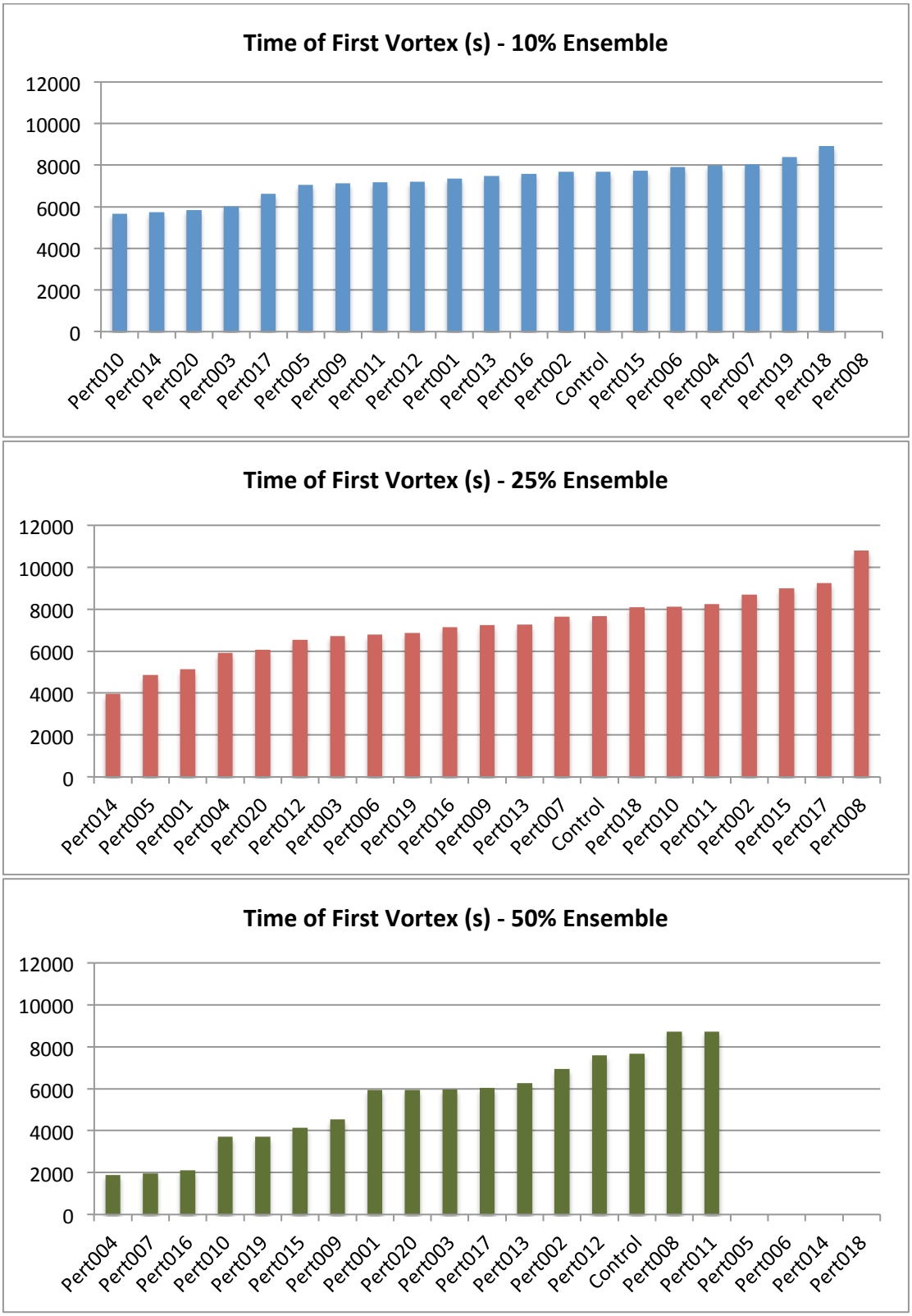

Figure 18. Time of first detected vortex for each simulation.

Figure 18 shows that the time of first detection varies more widely as the magnitude of the perturbations increases. The 10% ensemble ranges from 5670 s to 8910 s, and the 25% ensemble ranges from 3960 s to 10800 s. In the 50% ensemble, the times vary from 1890 s to 8730 s, which spans the same length of time as the 25% ensemble. Although the range did not differ between these two ensembles, the detections overall occur earlier in the 50% ensemble. This is consistent with a decrease in the earliest time of first detection as the perturbation magnitudes increases across the three ensembles.

While the control sounding is conducive to tornado generation, it appears that applying various perturbations can improve it further by allowing earlier development. This is probably due in part by alteration of the convective inhibition (CIN), lower values of which would allow the storm to develop more rapidly. The relationship between various sounding parameters that vary in response to the applied perturbation will be investigated in greater depth in later sections.

4.2.4 Tangential Wind Speed

The VDAC output includes a calculation of the tangential wind speed V_T of each vortex at the radius assessed by the algorithm. Vortices were required to have a tangential wind speed of at least 15 ms^{-1} in order to be recorded in an effort to reduce detections of weak spin-ups.

The histograms of the tangential wind speed observed for all vortices in each ensemble, normalized by the ensemble size, are shown in Figure 19. All of the ensembles favor vortices with weaker wind speed, although the 25% and 50%

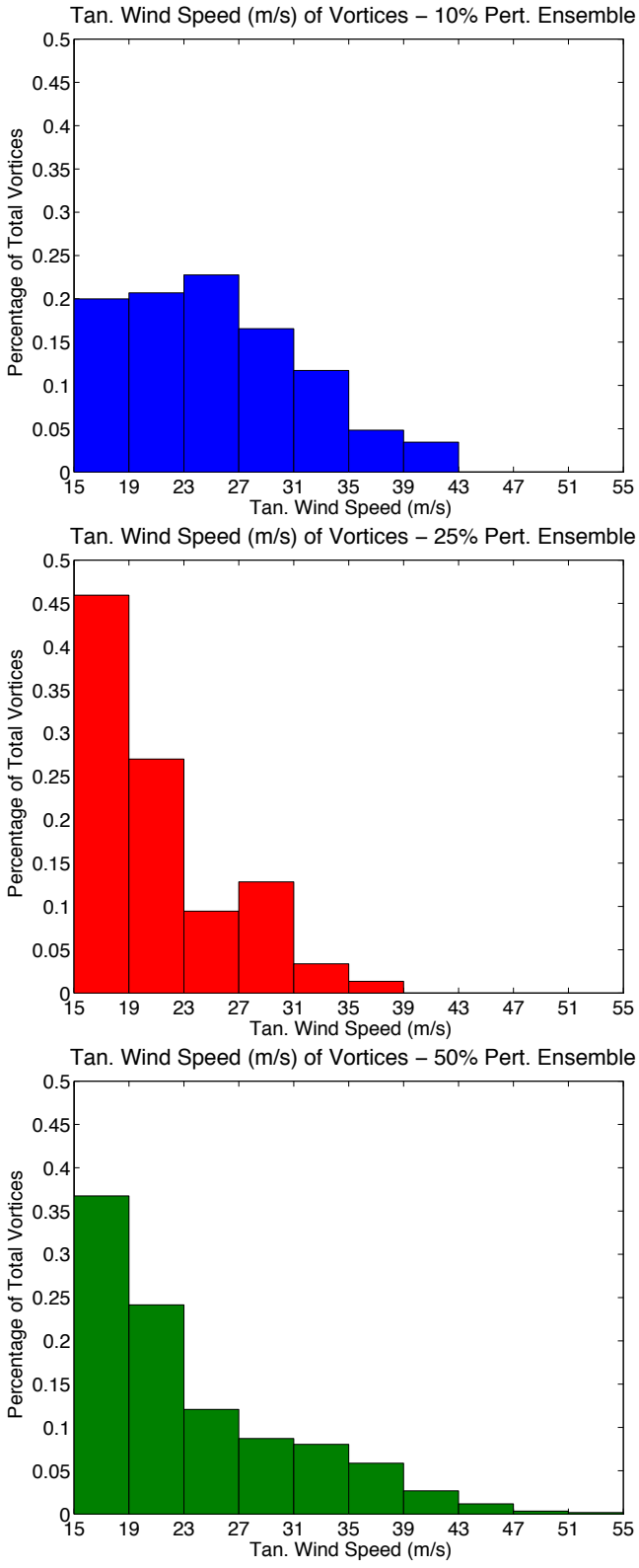

Figure 19. Histograms of tangential wind speed of all vortices detected in each ensemble, normalized by the total number of vortices.

Table 3. P-values for K-S test of tangential wind speed distributions between each ensemble pair.

Ensemble Pair	P-value ($\alpha = 0.05$)
10% & 25%	3.57×10^{-8}
10% & 50%	3.58×10^{-5}
25% & 50%	3.32×10^{-3}

ensembles skewed more toward the 15-19 m s^{-1} bin, while the 10% ensemble produces a nearly uniform distribution across the lowest four bins (15-27 m s^{-1}). Of the three, the 50% ensemble appears to yield the smoothest curve and includes more vortices with larger tangential wind speeds than the other ensembles. The greatest tangential wind speed is 39.95 m s^{-1} for the 10% ensemble, 36.68 m s^{-1} for the 25%, and 51.13 m s^{-1} for the 50%.

A two-sample Kolmogorov-Smirnov (K-S) test was used to test the similarity of the tangential wind speed distributions between each ensemble. The null hypothesis is that the two samples are part of the same distribution, and the confidence interval was set to 95%. Based on the p-values in Table 3, none of the distributions were found to be statistically similar to the other two ensembles.

4.2.5 Circulation

An alternative metric of vortex strength is circulation, which includes both the tangential velocity and radius of the vortex. Circulation C is given by

$$C = \oint_C \mathbf{V} \cdot d\mathbf{l}$$

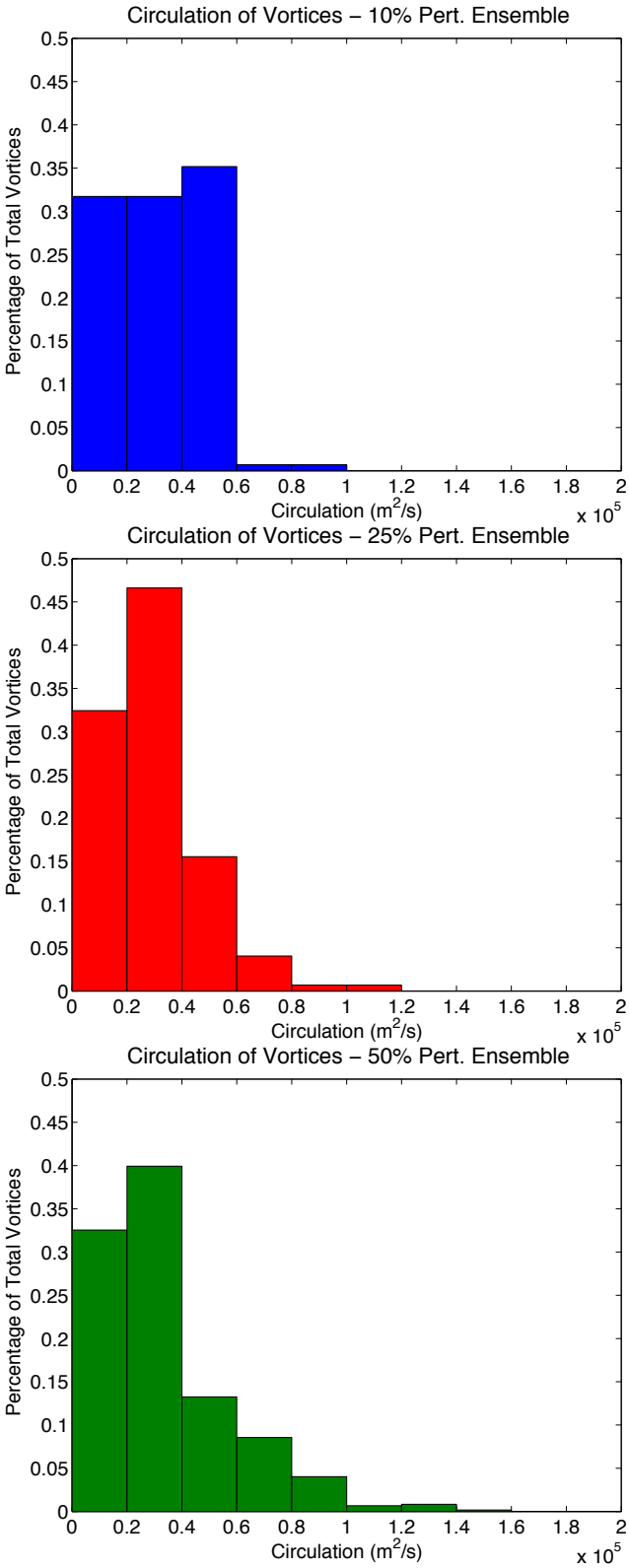

Figure 20. Histograms, normalized by total vortex count, of vortex circulation for 10%, 25%, and 50% ensembles.

where **V** is the velocity vector integrated along a closed curve. By Stokes' Theorem, the circulation may be written in terms of vorticity as

$$C = \oint_A \zeta \, dA = \zeta \, A$$

where the vertical vorticity, ζ, is summed over the area of the vortex. Since the detected vortices in the simulations are assumed to be circular, the form

$$C = \mathbf{V_T} A = 2\pi \mathbf{V_T} r,$$

where $\mathbf{V_T}$ is the tangential wind speed and r is the radius of the vortex, is used to compute the circulation for each detection.

Histograms of the circulation of all vortices in each ensemble through t = 7200 s, normalized by total vortex count, are contained in Figure 20. The majority of vortices in all ensembles have circulations below 6 x 10^4 m^2 s^{-1}, but the proportion of vortices with a circulation greater than 6 x 10^4 m^2 s^{-1} increases along with the size of the perturbations. The p-values for the K-S comparisons in Table 4 show that the 10% ensemble distribution is significantly different from the other two ensembles, but the difference is not significant between the 25% and 50% ensembles.

Table 4. P-values for K-S test of circulation distributions for each ensemble pair.

Ensemble Pair	**P-value (α = 0.05)**
10% & 25%	0.036
10% & 50%	0.004
25% & 50%	0.204

4.2.6 Vortex Radius

Figure 21 contains histograms, normalized by the total vortices in the ensemble, of the radius of all detections within each of the three ensembles. The minimum allowed radius for the vortex detections was 100 m, which is equal to the horizontal grid spacing. Each of the distributions is skewed toward vortex sizes smaller than 300 m, with a general decrease in the percentage of vortices as the radius increases. In this case, the 25% ensemble produces a smoother curve. More vortex sizes fell around 500 m in the 25% and 50% ensembles compared to the 10%.

A few anomalies occur in the higher radius values. Only the 10% and 50% ensembles contained vortices with radii in the 900-1000 m range, and the 10% ensemble had a slightly greater percentage of its detected vortices in this range than the50%. The 10% ensemble also did not produce any vortices in the 500-900 m range, unlike the 50% ensemble. The maximum detected vortex radius for each ensemble was 951 m, 702 m, and 915 m for the 10%, 25%, and 50% ensembles.

The Kolmogorov-Smirnov comparisons with 95% confidence show that the 10% ensemble distribution is not statistically similar to the other ensembles, but there is some doubt as to the difference between the 25% and 50% ensembles since the p-values were not small enough to reject the null hypothesis that the pairs are similar (Table 6). While there are statistical differences between the tangential wind speed distributions, there does not appear to be a specific trend based on the ensemble perturbation magnitude.

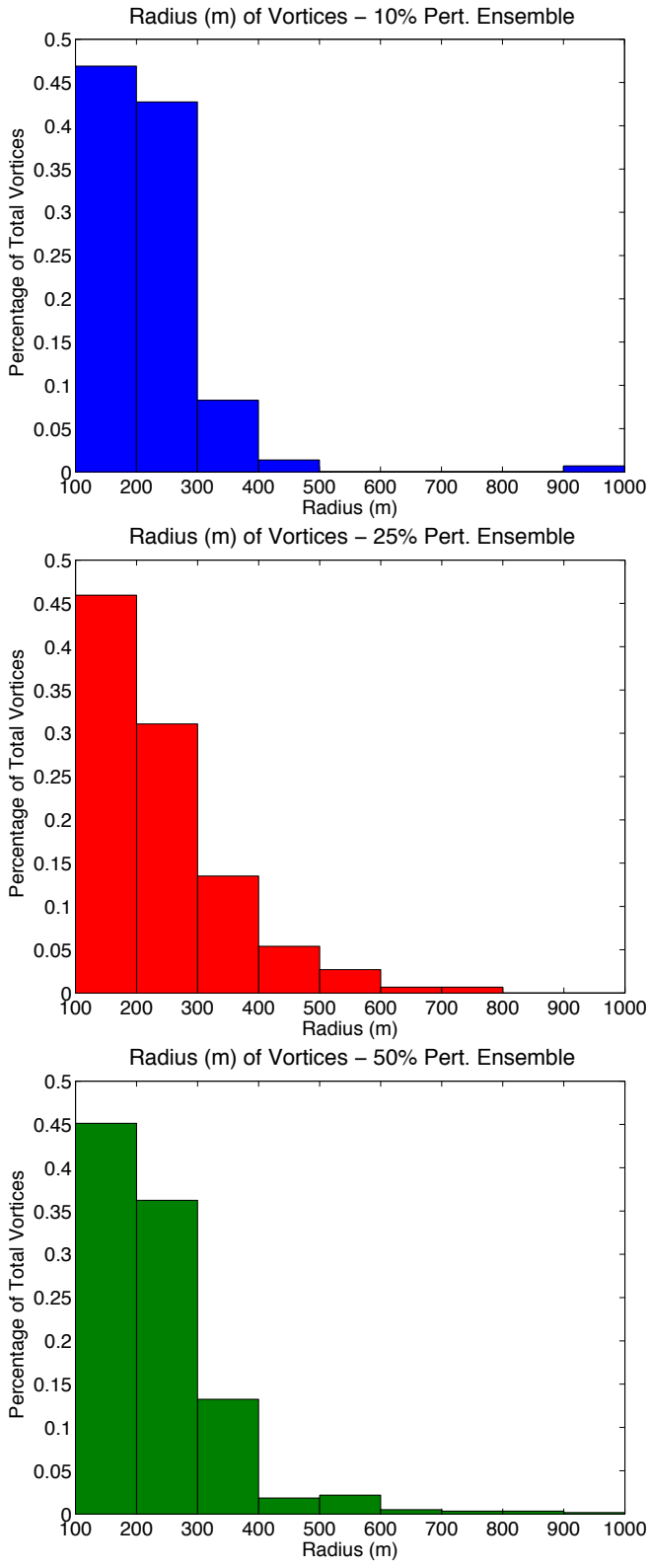

Figure 21. Histograms of radius size of detected vortices in each ensemble, normalized by total number of vortices.

Table 5. P-values for K-S test of tangential wind speed distributions for each ensemble pair.

Ensemble Pair	P-value (α = 0.05)
10% & 25%	0.031
10% & 50%	0.050
25% & 50%	0.221

4.2.7 Comparison of Radius to Tangential Wind Speed

The scatter plots in Figure 22 depict the distribution of the tangential wind speed relative to the size of the detected vortices. There are a variety of detected tangential wind speeds at each radius, indicating that there is not a strong correlation between the two variables. This observation is corroborated by the Pearson correlation coefficients calculated for radius and tangential wind speed, which are -0.025, -0.055, and 0.228 for the 10%, 25%, and 50% ensembles, respectively. These values are well below 0.5, which reflects the lack of a significant linear trend in the data.

Despite the lack of correlation, some commonalities in the pattern of the distribution can be observed. For all three ensembles, the greatest density of points is located in the lower left corner of the plots, suggesting that most detected vortices were relatively small and weak. The strongest vortices in terms of tangential wind speed also tend to fall between 200 and 300 m in each ensemble, although there is not as clear of a distinction in the 25% ensemble. Given that there are very few total points above about r = 600 m, it is difficult to establish a true trend among the larger vortices. However, none of the detected vortices with a radius greater than 600 m had a tangential wind speed as high as that of the strongest vortices with smaller radii.

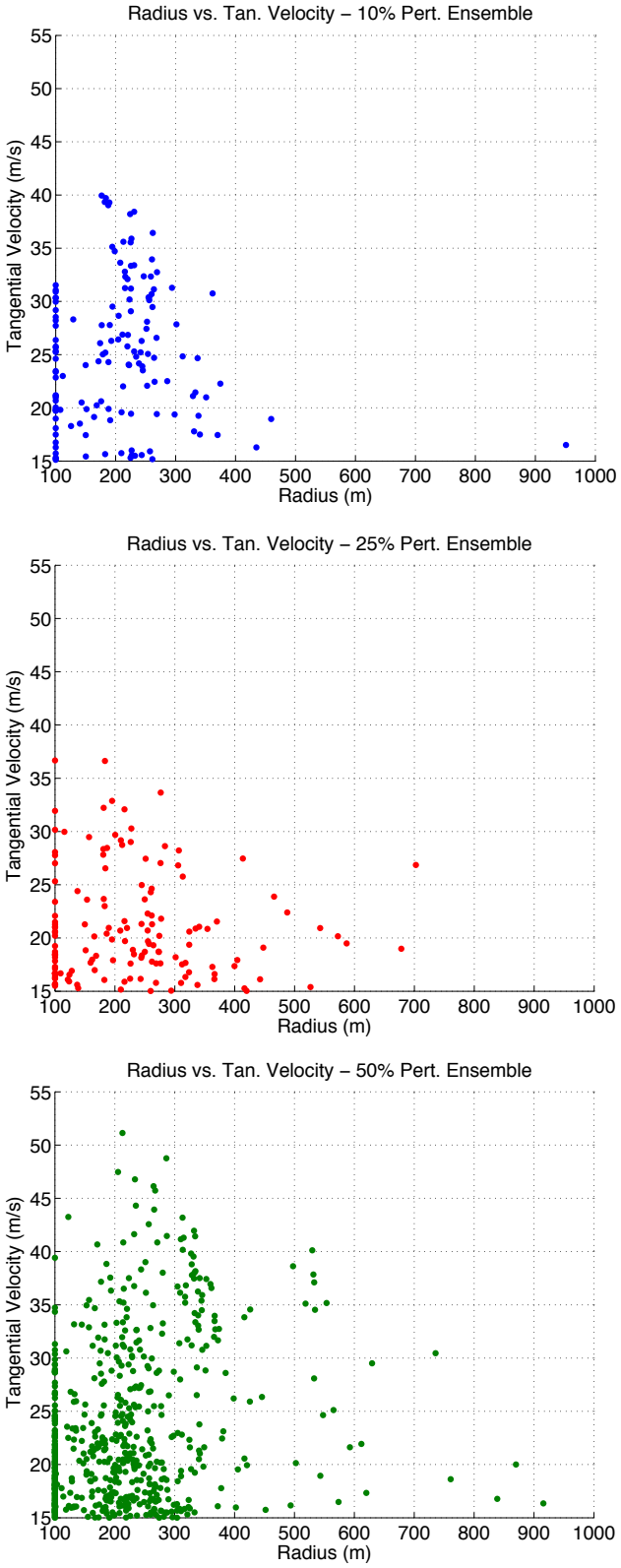

Figure 22. Scatter plot of tangential velocity vs. radius for all detected vortices in each ensemble.

4.3 Relationship of Vortex Characteristics to Initial Environment

4.3.1 Time of First Detected Vortex

To determine whether any linear relationship existed between the initial storm environment for each ensemble member and the time at which the first vortex that met the criteria was observed, the Pearson correlation coefficient was calculated between the time of the first vortex detection and the various sounding parameters described in the Methodology section. As in the analysis in Section 4.2, ensemble members that either did not produce any vortices during the course of the full three-hour simulation or produced them after erroneous precipitation was triggered by boundary interactions were excluded from the analysis. In order to be considered significant, the absolute value of the correlation coefficient was required to exceed 0.6. The points used in the calculation were also plotted so that the calculated values could be assessed for accuracy by inspection (Figure 23). Sounding parameters were calculated with mixed layer (ML) parcels from the lowest 100 hPa of the atmosphere.

In the 50% ensemble, there is a weak positive trend between the ML lifting condensation level (LCL) and time of first detection based on the correlation coefficient of 0.36, but little visual indication of this is present in the scatter plots. Correlation coefficients of 0.73 and 0.66, respectively, reflect strong positive trends between the time of first detection and the level of free convection (LFC) and convective inhibition (CIN). Negative trends exist for the equilibrium level (EL, not shown) and convective available potential energy (CAPE).

The correlations between the sounding parameters and time of first detection in the 25% ensemble are similar to those in the 50% ensemble, except that the correlation

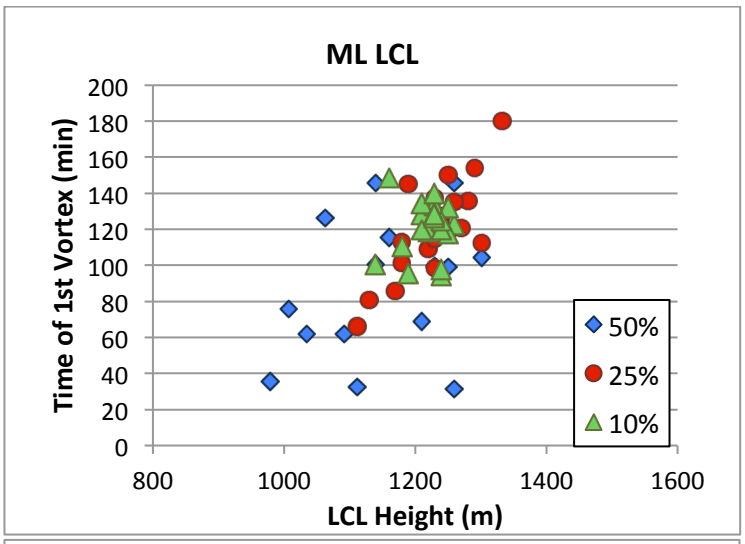
ML LCL
Time of 1st Vortex (min)
200
180
160
140
120
100
80
60
40
20
0
800
1000
1200
1400
1600
LCL Height (m)
50%
25%
10%

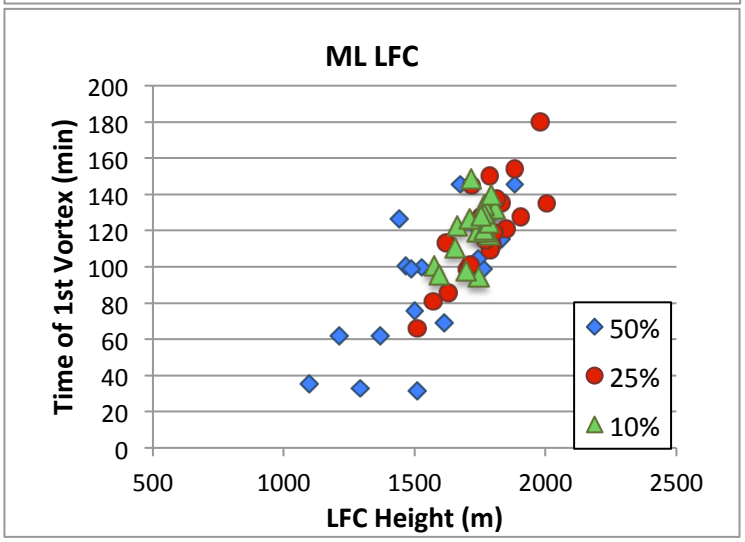
ML LFC
Time of 1st Vortex (min)
200
180
160
140
120
100
80
60
40
20
0
500
1000
1500
2000
2500
LFC Height (m)
50%
25%
10%

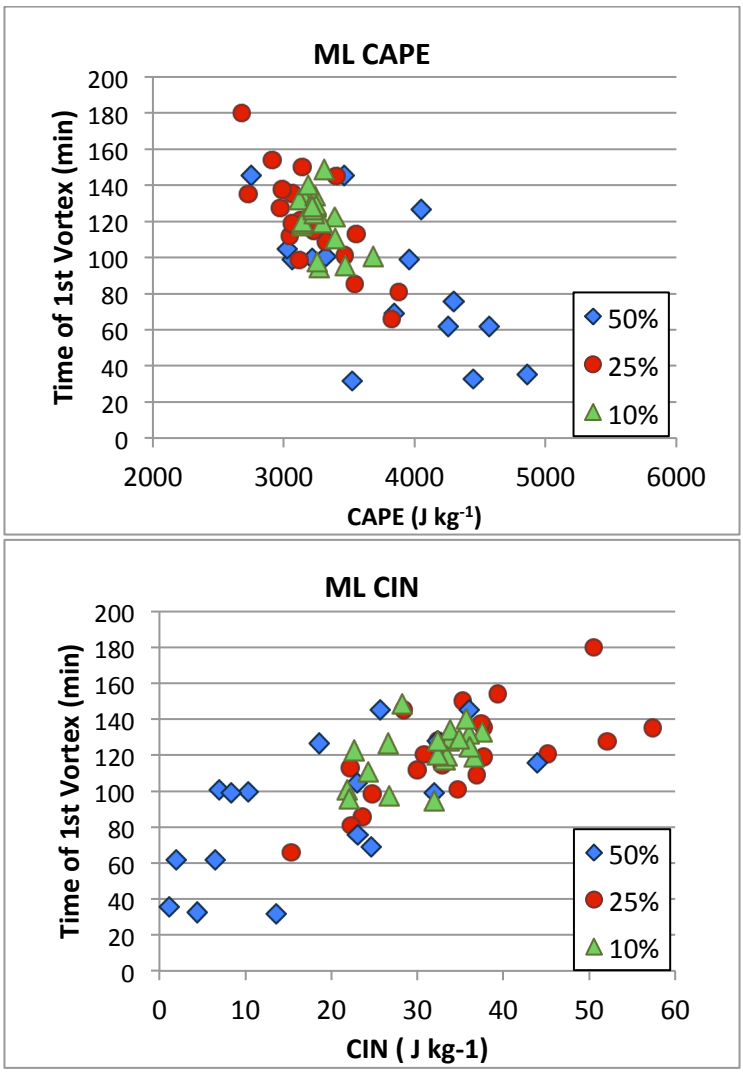

Figure 23. Scatter plots of time of first detected vortex vs. mixed layer LCL, LFC, CAPE, and CIN for each ensemble member.

coefficient for the ML LCL is much stronger at 0.78. In the 10% ensemble, the points are clustered within a narrower range of values and, as such, have low correlation coefficients. However, when the points from all three ensembles are overlaid for each variable, they appear to fall within the same general swath (Figure 23). This suggests that the trends are robust from ensemble to ensemble.

The trends exhibited in the data reflect what would be expected from a thermodynamic standpoint. As discussed in the literature review, a high value for CAPE and low value for CIN is considered to be a prime combination for supercell development. CAPE is integrated between the LFC and EL. If these two values were lowered and heightened, respectively, this would result in a greater depth for the integration and, potentially, a greater degree of CAPE in the environment. An additional consideration for tornadic potential is the vertical distribution of CAPE, with a greater concentration near the surface being more beneficial for low-level storm dynamics than if it were spread within a narrower, deeper area in the sounding. The relationship between the time of first detection and CIN can be explained by the fact that a lower value of CIN allows convection to develop more rapidly, which could decrease the amount of time the storm requires to reach a mature state and produce strong, low-level vortices.

4.3.2 Maximum Tangential Velocity

A comparison between the sounding parameters and the maximum tangential velocity of any vortex retrieved during the 0-7200 s analysis time period for each ensemble member is plotted in Figure 24. The thermodynamic parameters were

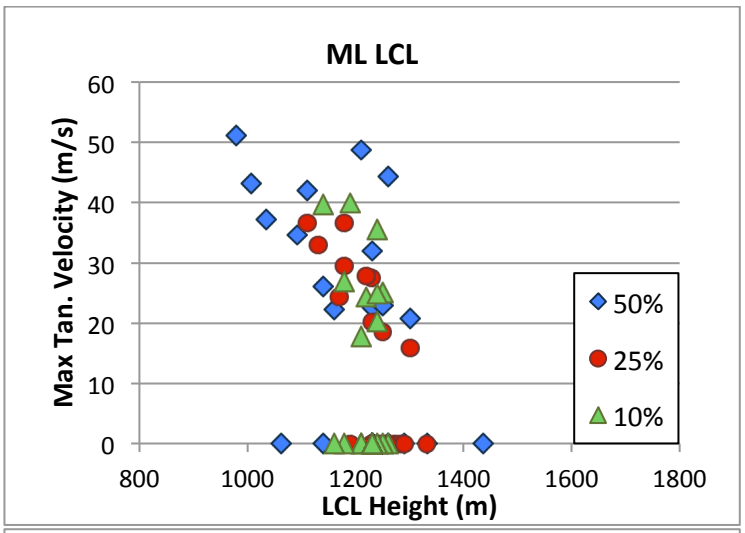
ML LCL
Max Tan. Velocity (m/s)
60
50
40
30
20
10
0
800
1000
1200
1400
1600
1800
LCL Height (m)
50%
25%
10%

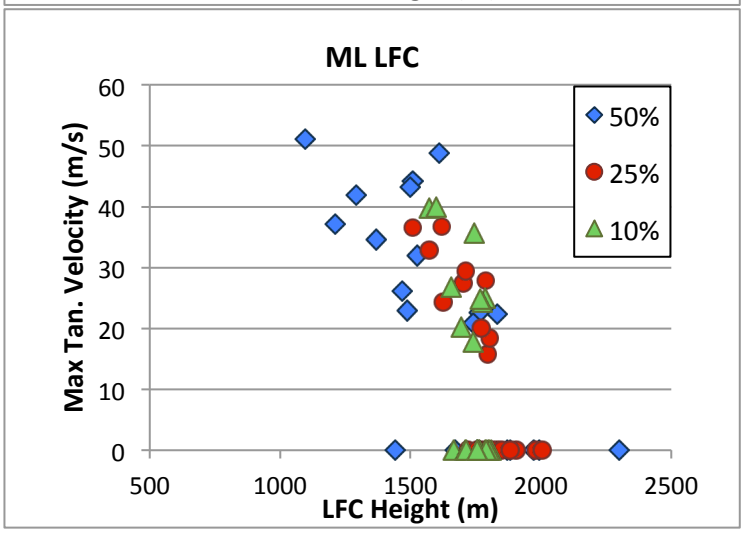
ML LFC
Max Tan. Velocity (m/s)
60
50
40
30
20
10
0
500
1000
1500
2000
2500
LFC Height (m)
50%
25%
10%

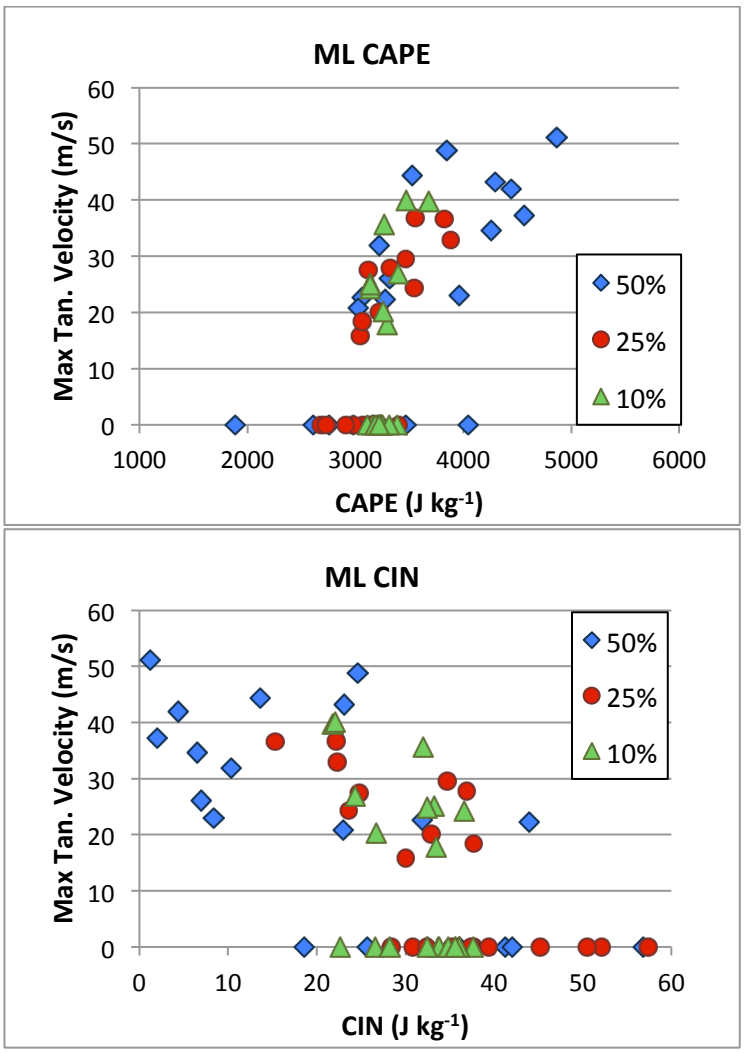

Figure 24. Scatter plot of maximum detected vortex tangential velocity per ensemble member and mixed layer LCL, LFC, CAPE, and
CIN of initial environment.

calculated by using a mixed layer parcel. Ensemble members that did not produce any detectable vortices are denoted by points with 0 m s^{-1} maximum velocity. Trends in the data are similar to the results from the time of first detected vortex. Changes in the LCL were not well correlated with the maximum tangential velocity. However, the maximum tangential velocity of the detected vortices did decrease somewhat with higher LFC and CIN values. A lower LFC would allow air parcels to realize the CAPE with less attendant lift required, aiding in more rapid storm development and ability to organize the energy required for faster wind speeds in vortices. Greater convective inhibition would suppress storm development, which would likely delay or completely inhibit vortex development. Since the only vortices that were gathered occurred in the first 7200 s of simulation time, it is probable that the distribution would change if the simulations were given more time to produce vortices.

Of the vortices that developed in the analysis time, the maximum tangential velocity tended to increase with higher CAPE. As shown in Figure 24, virtually all of the ensemble members with CAPE exceeding 4000 J kg^{-1} produced vortices within the given time span. In addition, their maximum velocities were among the highest from all simulations.

4.3.3 Maximum Radius

Correlations between maximum observed radius and sounding parameters for each ensemble within the analysis time (Figure 25) closely resembled those found in the maximum tangential velocity (Figure 24). The best correlations exist with the LFC and CAPE, with maximum radius tending to be higher for soundings with lower LFCs and

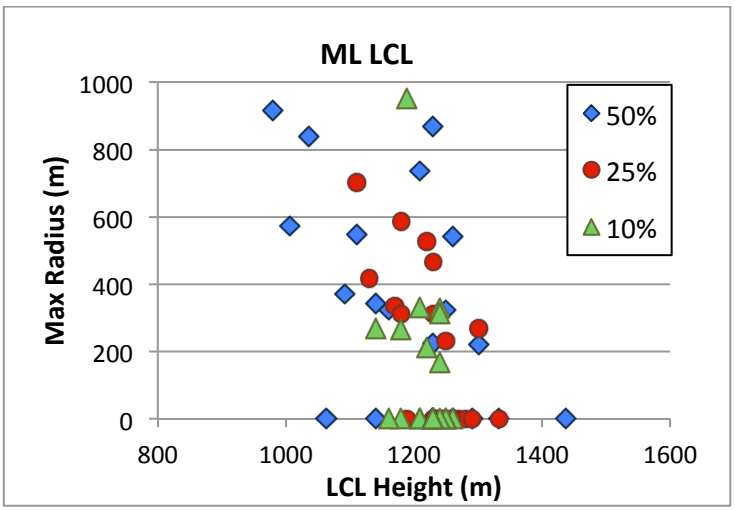
ML LCL
Max Radius (m)
1000
800
600
400
200
0
800
1000
1200
1400
1600
LCL Height (m)
50%
25%
10%

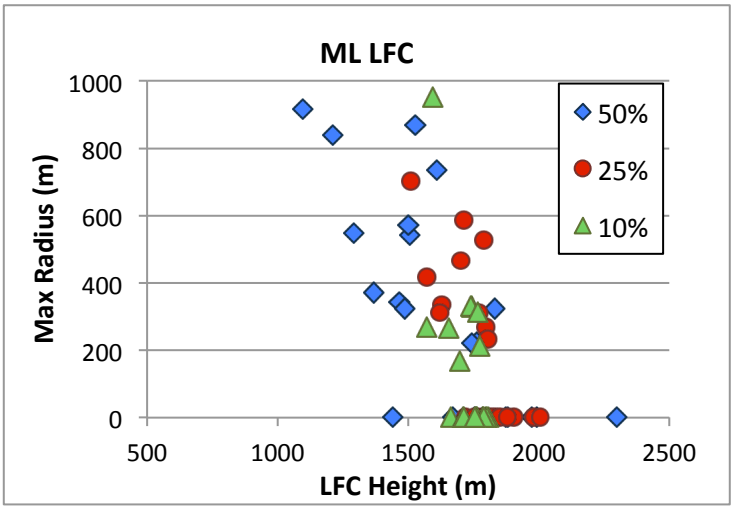
ML LFC
Max Radius (m)
1000
800
600
400
200
0
500
1000
1500
2000
2500
LFC Height (m)
50%
25%
10%

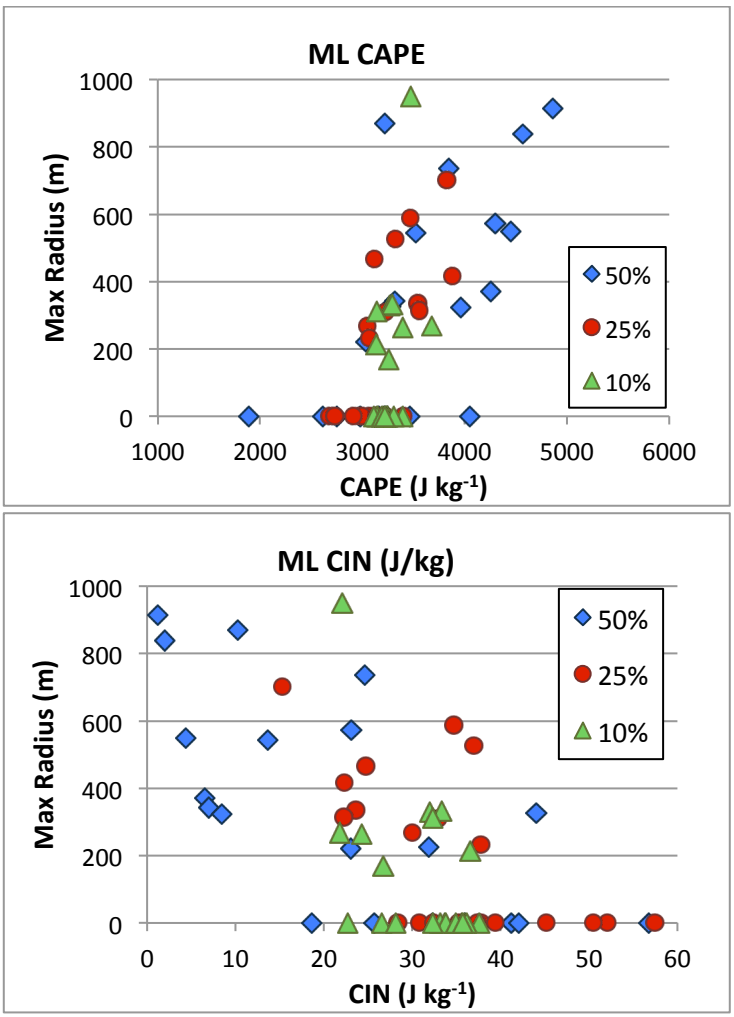

Figure 25. Scatter plot of maximum detected vortex radius per ensemble member and mixed layer LCL, LFC, CAPE, and CIN of initial environment.

greater CAPE. Lower CIN was also associated with larger maximum radii. Again, the LCL did not bear a strong correlation to the vortex radius.

4.4 Case Study: Effects of Environment on Cold Pool Formation

The previous analysis indicates that the calculated parameters from the perturbed soundings are generally related to the characteristics of the vortices generated in the corresponding simulations. However, it does not provide any information about the specific processes by which the background environment affects storm behavior. This section examines processes that may hinder or enhance the genesis of low-level rotation by analyzing model variables near the surface and aloft for simulations that did and did not produce vortices in the simulation.

4.4.1 Initial Conditions

Six of the 50% perturbed soundings were selected for further analysis based on the time of the first detected vortex, as well as the persistence of the vortices with time. The vortex-producing ensemble members are Pert007, Pert010, and Pert019; those that did not produce detectable vortices are Pert006, Pert014, and Pert018. These soundings are overlaid in Figure 26 and colored according to group, with blue and orange for the vortex-producing storms and green and red for the non-producing storms.

The most consistent distinction between the two groups occurs in the dew point profiles below 850 hPa. Boundary layer moisture is 3-5 K greater in the perturbations that produced early vortices compared to those that produced none. The large spread in dew points in the mid-to-upper levels that was noted in the composite of all perturbations in

the 50% group is apparent in this composite also, but there is no clear delineation between the profiles from the two selected groups. In fact, the moisture profile above 400 hPa for one of the non-producers is almost identical to that of one of the early producers. From 600-500 hPa, the average moisture profile is about 2 K drier for the non-producing

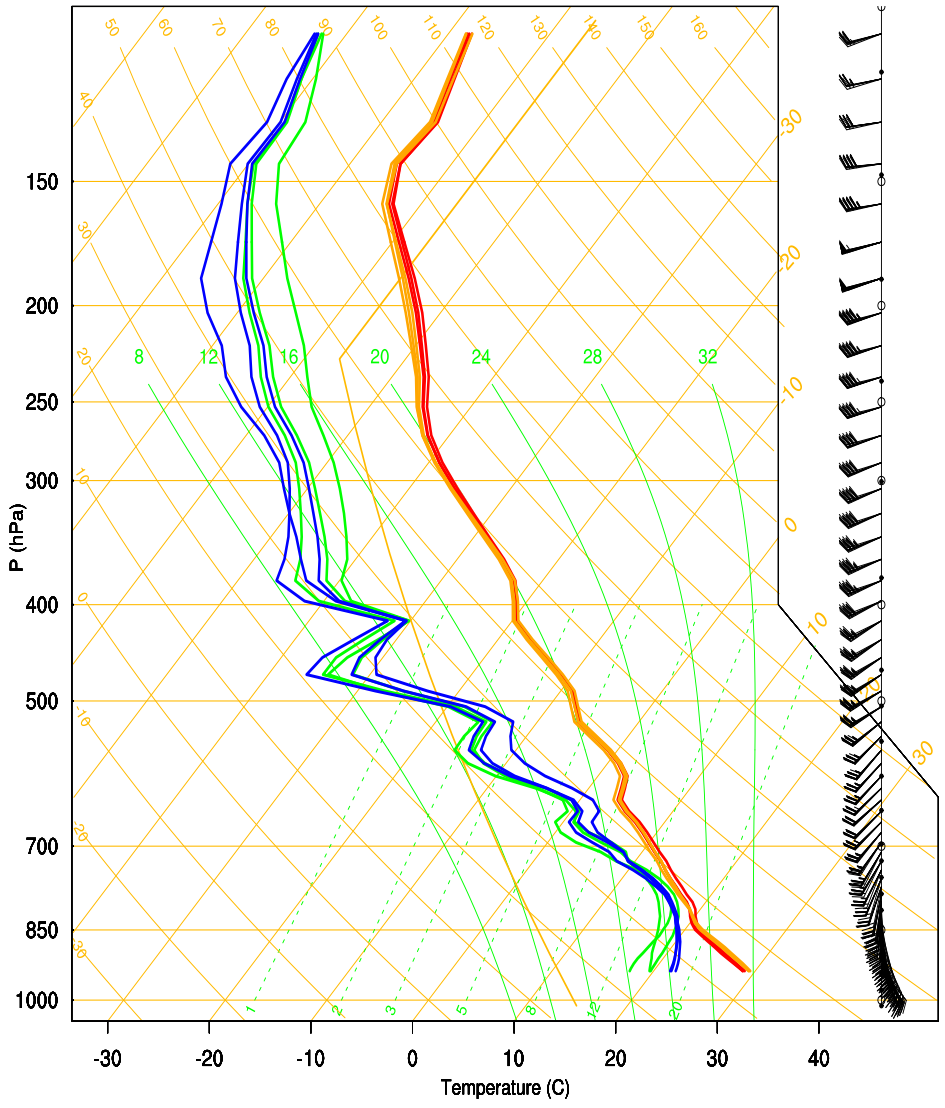

Figure 26. Initial soundings of six members of the 50% error ensemble. Simulations that failed to produce vortices (Pert006, Pert014, and Pert018) are plotted in green and red. Simulations that produced vortices within the first hour of model time (Pert007, Pert010, and Pert019) are plotted in blue and orange.

group than for the early producers, but there is still quite a bit of overlap of the individual profiles from the two groups. These observations seem to confirm that boundary layer thermodynamics are important to the storm's ability to generate low-level vortices.

The mixed layer values of the LCL, LFC, CAPE, and CIN for each environment are listed in Table 6. CAPE in the vortex-producing environments is greater by 1500-2000 J kg^{-1}, which enhances the theoretical maximum updraft in developing storms. CIN is also much lower than in the ensemble members that did not produce detectable vortices. This has implications not only for the potential strength of the updraft but also for the ability of the downdraft to reach the surface. Given the importance of the rear flank downdraft in the development of tornadoes, increased CIN could negatively impact vortex production.

The hodographs for the selected ensemble members are shown in Figure 27 with the nonproducing environments in red, vortex-producing environments in blue, and the

Table 6. Thermodynamic convective parameters for selected ensemble member environments. Simulations that produced vortices are shaded in light grey.

Ensemble Member	LCL (m)	LFC (m)	CAPE (J/kg)	CIN (J/kg)
Pert006	1291	1972	2608	42
Pert014	1230	1992	2980	57
Pert018	1437	2301	1888	83
Pert007	1111	1291	4447	4.4
Pert010	1092	1368	4253	6.5
Pert019	1035	1211	4566	2.0

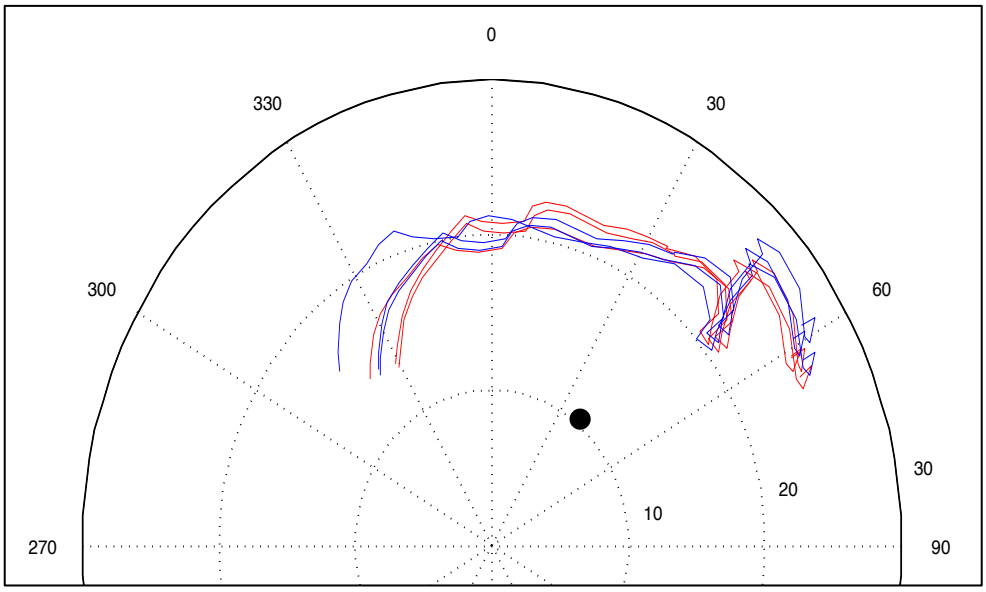

Figure 27. Overlay of hodographs from the vortex-producing (blue) and non-producing (red) simulations. The estimated storm motion is indicated by the black marker.

estimated storm motion indicated by the black marker. They largely follow the same shape, although Pert010 has markedly stronger winds in the lowest 1 km compared to the other environments. Using the grid motion as the estimated storm motion, SRH for the 0-1 km and 0-3 km layers were calculated, along with the total shear integrated over the 0-1 km layer (Table 7). Unlike with the thermodynamic parameters, there does not appear to be a consistent trend in the shear parameters that corresponds to vortex production. The 0-1 km SRH is a little lower in the vortex-producing storm environments, while the 0-3 km SRH is higher. The total shear is similar between the two groups.

4.4.2 Cold Pool Potential Temperature

As discussed in the literature review, the cold pool in the rear flank of the storm appears to be an important contributor to the process of tornadogenesis. The relative strength of the cold pools in the selected simulations was assessed using the perturbation

Table 7. Shear parameters for selected ensemble member environments. Simulations that produced vortices are shaded in light grey.

Ensemble Member	SRH 0-1 km ($m^2 s^{-2}$)	SRH 0-3 km ($m^2 s^{-2}$)	Total Shear 0-1 km ($m s^{-1}$)
Pert006	73.6	322.7	12.5
Pert014	77.1	328.0	12.8
Pert018	68.9	331.9	12.5
Pert007	64.9	319.8	12.0
Pert010	66.0	359.5	12.3
Pert019	71.1	343.1	12.3

potential temperature (θ') field at 100 m AGL during the first 65 min of simulation time. In cases where the parent supercell split during the analysis time period, the search domain was adjusted to exclude any areas where the cold pool from the left split had spread, ensuring that the analysis was focused on the initial right-moving supercell only.

The greatest overall θ' deficits over time occurred in the vortex-producing storms, where the minimum θ' fell below -3 K (Figure 27). The non-producing simulations generally remained warmer than -2 K. In addition to the difference in overall minimum θ', the slopes of the time series are similar within each group. Each of the non-producing simulations steadily decreases before becoming relatively constant, whereas the minimum θ', in general, decreases persistently over time among the vortex-producing group.

The placement of the cold pool relative to the edge of the 30 dBZ simulated reflectivity contour at z = 1 km AGL follows a pattern according to storm type as well.

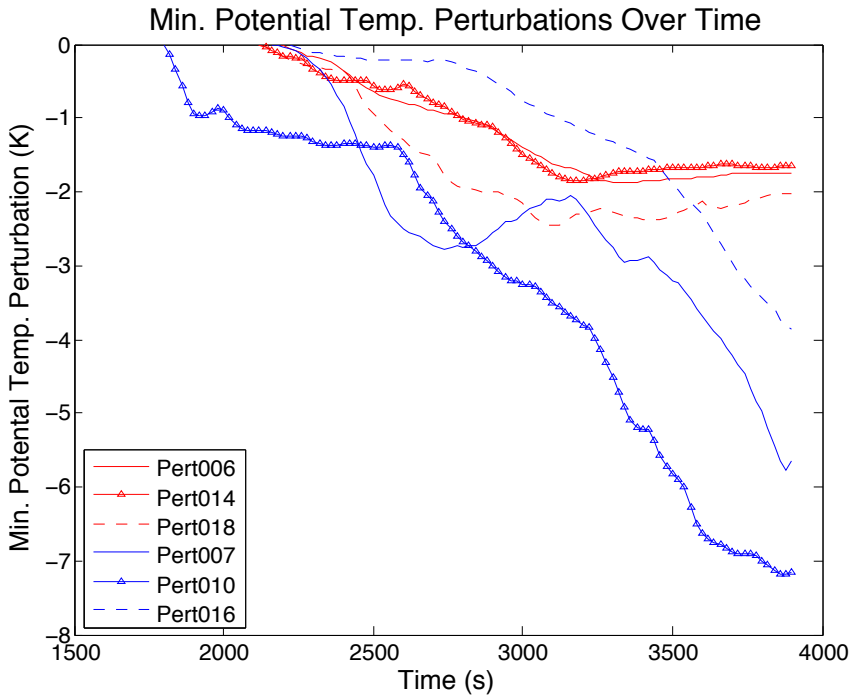

Figure 27. Minimum θ' value in the vicinity of the right-moving supercell in each simulation. Blue indicates vortex-producing simulations, and red represents non-producing simulations.

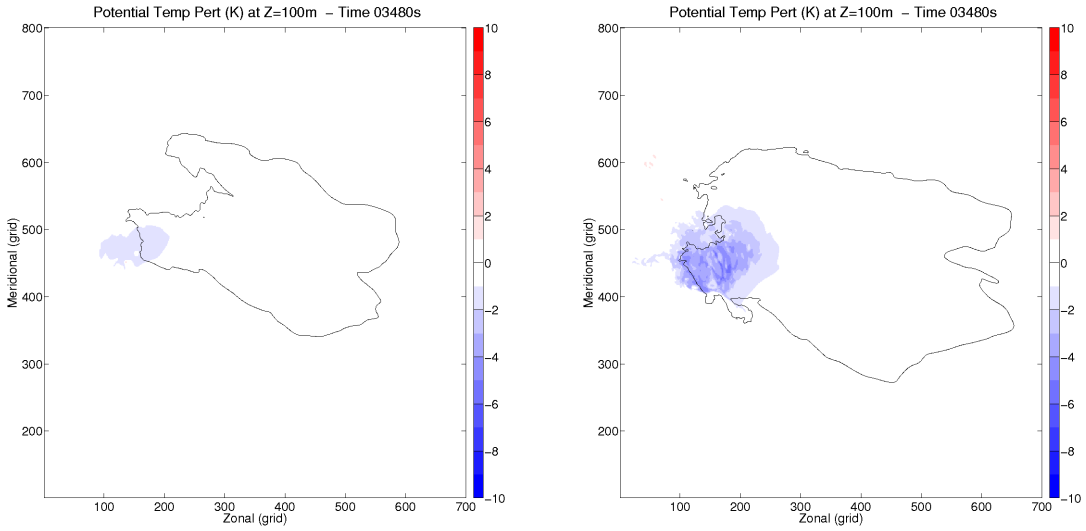

Figure 28. Comparison of the extent of the cold pool as shown by θ' field at z = 100 m AGL for non-producing Pert006 (left) and vortex-producing Pert010 (right) at t = 3480 s.

Figure 28 shows an example from each of the two groups. The cold pool in the vortex-producing storms (right) remains within the bounds of the reflectivity contour, while the cold pool is displaced to the north and west in the non-producing storms (left). Since the downdraft associated with this cold pool must wrap around the updraft in order to enhance low-level rotation, it appears that, in the non-producing simulations, the downdraft is too far away and/or too weak to do this effectively.

4.4.3 Relative Humidity

As air descends within the RFD, it is adiabatically warmed with an attendant decrease in relative humidity. Relative humidity (RH) is a measure of moisture in the air as a function of the temperature. In comparing the relative humidity fields at z = 100 m AGL (not shown), the distinguishing feature between the two groups of simulations was the appearance of an area of negative RH perturbations (relative to the storm environment) in the rear flank of the storm. For all simulations, an area of positively perturbed RH develops throughout the rear flank after storm initiation, presumably as a result of evaporating precipitation. Only the vortex-producing simulations also develop an area of negatively perturbed RH that spreads outward over time. Vortex development in Pert010 and Pert019 appears to occur after the –RH' has expanded southward. The relationship between the –RH' and timing of the detected vortices is less clear in Pert007. The areas of –RH' roughly coincide with areas of $+\theta'$ in time, which suggests that dry air is becoming entrained into the RFD and warming adiabatically.

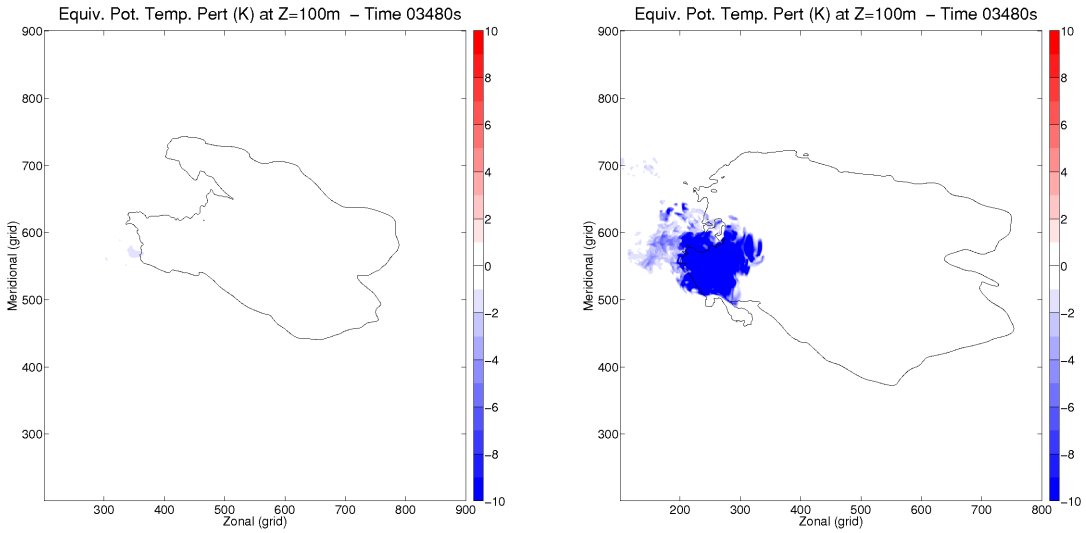

Figure 29. Comparison of equivalent potential temperature (θ_e) of cold pool at z = 100 m AGL for non-producing Pert006 (left) and vortex-producing Pert010 at t = (right) at t = 3480 s.

4.4.4 Equivalent Potential Temperature

The equivalent potential temperature, θ_e, is a function of both the temperature and the mixing ratio, which reflects the buoyancy of the air. Plots of the θ_e field for non-producing Pert006 and vortex-producing Pert010 are shown in Figure 29. The θ_e deficits in the vortex-producing simulations were greater than the θ deficits, indicating that the cold pools in these storms were both colder and drier compared to the non-producing storms. This agrees with Naylor and Gilmore (2014), who found that their tornadic supercell simulations had greater cold pool θ_e deficits than those that were non-tornadic.

4.4.5 Precipitation

The rainwater mixing ratio, q_r, at z = 2 km AGL was used as an estimate of how much liquid precipitation reached the lowest levels of the storm, i.e., how much

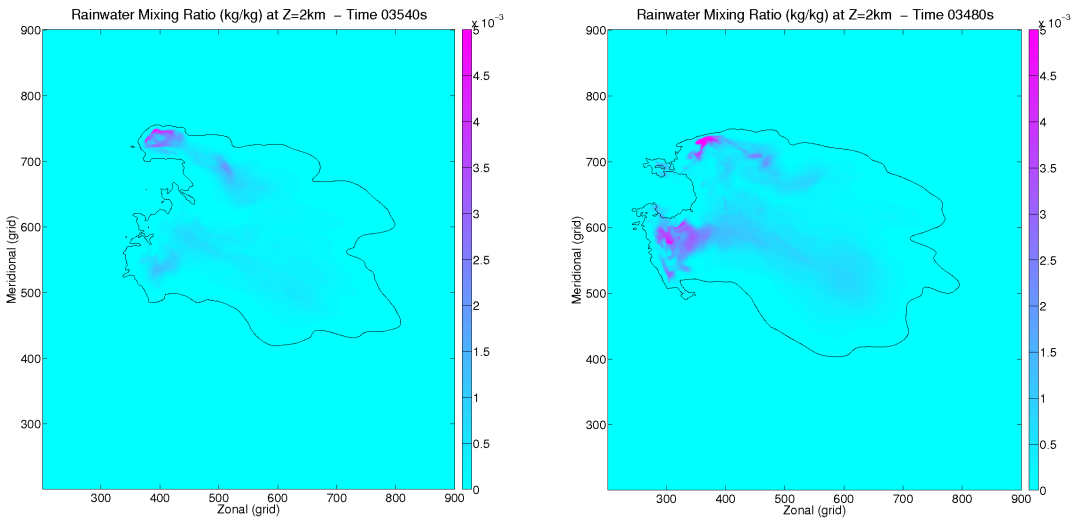

Figure 30. Comparison of rainwater mixing ratio (q_r) fields at z = 2 km AGL in non-producing simulation Pert018 (left) and vortex-producing simulation Pert019 (right).

evaporation occurred aloft rather than near the surface, where it could enhance the cold pool. Frozen precipitation was neglected. In the vortex-producing simulations, elevated values of q_r were present over a greater area of the storm, while the no-vortex storms exhibit overall lower q_r (Figure 30). Assuming a similar amount of rain is precipitating from the storm in all simulations, this suggests that more evaporation is occurring in the low- to midlevels of the no-vortex storms, which reduces evaporative cooling near the surface. This is consistent with the fact that the moisture profile in the storm environment is drier below 500 mb for the no-vortex storms compared to those that produced vortices.

Chapter 5: Conclusion

To determine the sensitivity of supercells and submesocyclone-scale vortices to typical mesoscale model forecast errors of winds, temperature, and humidity, a control sounding from a classic supercell environment was perturbed using 1-hour forecast errors observed within the RUC model on severe weather days (Cintineo and Stensrud 2013). Random draws from the observed errors, scaled to 10%, 25%, and 50% of their original magnitude, are used to generate 20 soundings from each scaled error magnitude. Using each perturbed sounding (and the control), a homogeneous domain environment is initialized on a large-eddy resolving grid (Dx, Dy ~100 m, Dz ~ 50 m), and 61 LES supercell simulations are generated over a three-hour integration period. Data mining of the simulation output every 30 seconds was accomplished using the Vortex Detection and Classification (VDAC) algorithm (Potvin 2013) to detect low-level vortices with tangential wind speed in excess of 15 m s^{-1} and to determine, using three specified levels between the lowest model grid level and 1 km, whether the vortex had vertical continuity. Continuity of vortices over time was not assessed.

The effect of the perturbations on storm evolution generally increased as larger magnitudes of errors were applied. The simulated reflectivity signatures for the 10% ensemble were similar to within 5 km of each other for the first 65 min of model time, including the representation of a left split storm that develops. Increasing the error magnitudes to 25% and 50% increase the divergence of the reflectivity and other field within each ensemble. This is clearly shown by a greater variation in the time of the development of the left-split cell across the ensemble.

The spatial envelope containing the detected vortices within each ensemble increases with increasing simulation time. By t = 7200 s, the majority of vortices fell within a swath perpendicular to the ensemble mean storm motion of approximately 6 km, 9 km, and 18 km for the 10%, 25%, and 50% ensembles, respectively. As with the reflectivity field, this is likely related to changes in storm-scale processes brought about by the environmental perturbations that may, in turn, affect the details of large storm-scale features (e.g., gust fronts, precipitation pulses) that generate low-level vortices.

The total number of vortices, tangential velocity, radius, and circulation during the first 3900 s of simulation time, as well as the time of the first detected vortex during the full three hours, were computed for each ensemble member and compared across the three ensembles. The distributions of total detected vortices from each ensemble member in the 10% and 25% ensembles did not differ significantly from each another, but both differed significantly from the 50% ensemble, which contained more variation among its members and overall larger vortex totals for those that produced vortices. Timing of the first vortex detection varied more widely for the 25% and 50% ensembles compared to the 10% ensemble, and the times of the earliest vortices decreased with larger environmental errors.

The overall distributions of the tangential velocity, radius, and circulation of all detected vortices within each ensemble differed from one another, but no clear pattern arose with relation to the magnitude of the environmental errors. Comparison of the maximum tangential velocity of all detected vortices from each ensemble showed a range of 19.7 m s^{-1}, 20.9 m s^{-1}, and 33.8 m s^{-1} for the 10%, 25%, and 50% ensembles, respectively. The ranges of maximum radius were likewise 291 m, 410 m, and 695 m.

Correlations between mixed layer convective parameters calculated from the initial environment and the time of first detected vortex, maximum tangential velocity, and maximum radius observed in each simulation were assessed by ensemble. Earlier vortex production is associated with greater CAPE, lower CIN, and lower LFCs, as is higher maximum tangential velocity and radius.

A case study of six of the 50% ensemble members, three that produced vortices early in the simulation and three that never produced vortices, was conducted to ascertain possible storm processes that could impact vortex production. Stronger cold pools formed in the storms that produced vortices compared to those that did not. This is similar to the results of Naylor and Gilmore (2014) and agrees with the finding of Naylor et al. (2012) that CIN reduces the strength of the downdraft in addition to the updraft. The rainwater mixing ratio at 2 km AGL was greater over a broader area in the vortex-producing simulations, which suggests that more evaporation may be occurring aloft rather than near the surface in the non-producing storms, consistent with their overall drier environmental moisture profile below 500 hPa. Further analysis of the three-dimensional variable fields in the case study is needed to improve understanding of how the rear flank of the storms is being affected by the small changes in the environment at all vertical levels.

The results indicate that vortex production in supercell simulations is sensitive to perturbations smaller than 1-hour forecast errors that are typical in the RUC model for severe convective environments. Given this sensitivity to errors, more accurate measurements of the atmosphere in areas where storms may develop is essential. Expanding the existing observation network in the CONUS could be beneficial in

reducing initial condition errors in operational forecast models. However, the results from this study seem to suggest that a threshold exists beyond which reduction of error in the initial conditions is unlikely to greatly improve the forecast. This situation is seen in cases where large differences appeared between the 50% ensemble and the 10% and 25% ensembles but the latter two were not significantly different from each other.

Overall, changes to the initial storm environment impacted the ability of supercells to produce low-level vortices, more so as the magnitude of the perturbations increased. This emphasizes the continuing need for an ensemble approach to forecasting. It may be possible to predict very general characteristics of tornadoes, such as whether they are likely to develop sooner or later after storm initiation or an estimate of where they may occur within an area O(100) km^2. However, many obstacles remain in predicting them even to that extent with current forecast models.

This study could be improved in several ways. Expanding the number of members in each ensemble may improve the quality of the statistics used to compare the ensembles by increasing the sample size to at least 30. Furthermore, applying the same methodology to additional control soundings could reveal whether the sensitivity to the environmental perturbations is similar to the results from the Geary sounding ensembles. It should be noted that multiple parameterizations that can have a profound impact on the representation of a supercell were held constant during this study. The results would likely differ with alterations to the microphysics parameters in the current scheme and/or use of another scheme altogether. Also of relevance is the impact of model resolution. The simulations included in this study were run at 100 m horizontal resolution, which is sufficient to resolve larger eddies, but even the most advanced plan for operational

forecast models to predict storms envision resolutions of ~1 km. As Δx increases, more turbulent kinetic energy must be approximated by the closure scheme, which increases error in the model. Future work may investigate sensitivity of low-level vortex generation to grid resolution to determine the impact of using a coarser, less expensive grid resolution that would be computationally feasible on a regional scale, instead of a higher resolution that better resolves turbulence and storm-scale dynamics.

References

Adlerman, E. J., K. K. Droegemeier, and R. Davies-Jones, 1999: A numerical simulation of cyclic mesocyclogenesis. *J. Atmos. Sci.*, **56**, 2045–2069.

Adlerman, E. J., and K. K. Droegemeier, 2002: The sensitivity of numerically simulated cyclic mesocyclogenesis to variations in model physical and computational parameters. *Mon. Wea. Rev.*, **130**, 2671–2691.

Baxter, M.A., 2011: Impacts of very small initial condition errors on mesoscale aspects of two cyclones. *Electronic J. Operational Meteor.*, **12** (1), 1–44.

Bei, N., and F. Zhang, 2007: Impacts of initial condition errors on mesoscale predictability of heavy precipitation along the Mei-Yu front of China. *Quart. J. Roy. Meteor. Soc.*, **133**, 83–99.

Brooks, H. E., C. A. Doswell, and R. A. Maddox, 1992: On the use of mesoscale and cloud-scale models in operational forecasting. *Wea. Forecasting*, **7**, 120–132.

Brooks, H. E., C. A. Doswell, and L. J. Wicker, 1993: STORMTIPE: A forecasting experiment using a three-dimensional cloud model. *Wea. Forecasting*, **8**, 352–362.

Browning, K. A., 1964: Airflow and trajectories within severe local storms which travel to the right of the winds. *J. Atmos. Sci.*, **21**, 634-639.

Bryan, G. H., and J. M. Fritsch, 2002: A benchmark simulation for moist nonhydrostatic numerical models. *Mon. Wea. Rev.*, **130**, 2917–2928.

Bryan, G. H., J. C. Wyngaard, and J. M. Fritsch, 2003: Resolution requirements for the simulation of deep moist convection. *Mon. Wea. Rev.*, **131**, 2394–2416.

Cintineo, R. M., and D. J. Stensrud, 2013: On the predictability of supercell thunderstorm evolution. *J. Atmos. Sci.*, **70**, 1993–2011.

Davies-Jones, R. P., 1982: A new look at the vorticity equation with application to tornadogenesis. Preprints*, 12th Conf. on Severe Local Storms*, San Antonio, TX, Amer. Meteor. Soc., 249-252.

Davies-Jones, R., 1984: Streamwise vorticity: the origin of updraft rotation in supercell storms. *J. Atmos. Sci.*, **41**, 2991–3006.

Davies-Jones, R. P., 1985: Dynamical interaction between and isolated convective cell and a veering environmental wind. Preprints, *14th Conf. on Severe Local Storms*, Indianapolis, IN, Amer. Meteor. Soc., 216-219.

Davies-Jones, R. P., D.W. Burgess, and M. Foster, 1990: Test of helicity as a tornado forecast parameter. Preprints, *16th Conf. Severe Local Storms*, Kananaskis Park, Alberta, Amer. Meteor. Soc., 588-592.

Davies-Jones, R., 2008: Can a Descending Rain Curtain in a Supercell Instigate Tornadogenesis Barotropically? *J. Atmos. Sci.*, **65**, 2469–2497.

Davies-Jones, R., and H. E. Brooks, 1993: Mesocyclogenesis from a theoretical perspective. *The Tornado: Its Structure, Dynamics, Prediction and Hazards*, *Geophys. Monogr.*, No. 79, Amer. Geophys. Union, 105-114.

Davies-Jones, R., R. J. Trapp, and H. B. Bluestein, 2001: Tornadoes and tornadic storms. *Meteorological Monographs*, **28**, 167–222.

Dawson II, D. T., M. Xue, J. A. Milbrandt, M. K. Yau, and G. Zhang, 2007: Impact of multi-moment microphysics and model resolution on predicted cold pool and reflectivity intensity and structures in the Oklahoma tornadic supercell storms of 3 May 1999. Preprints, *22nd Conf. on Weather Analysis and Forecasting/18th Conf. on Numerical Weather Prediction,* Salt Lake City, UT, Amer. Meteor. Soc., 10B.2.

Dawson, D. T., M. Xue, J. A. Milbrandt, and M. K. Yau, 2010: Comparison of evaporation and cold pool development between single-moment and multimoment bulk microphysics schemes in idealized simulations of tornadic thunderstorms. *Mon. Wea. Rev.*, **138**, 1152–1171.

Dawson II, D. T., L. J. Wicker, E. R. Mansell, and R. L. Tanamachi, 2012: Impact of the environmental low-level wind profile on ensemble forecasts of the 4 May 2007 Greensburg, Kansas, tornadic storm and associated mesocyclones. *Mon. Wea. Rev.*, **140**, 696–716.

Dawson, D. T., E. R. Mansell, Y. Jung, L. J. Wicker, M. R. Kumjian, and M. Xue, 2014: Low-level Z_{DR} signatures in supercell forward flanks: the role of size sorting and melting of hail. *J. Atmos. Sci.*, **71**, 276–299.

Deardorff, J. W., 1980: Stratocumulus-capped mixed layers derived from a three-dimensional model. *Bound.-Layer Meteor.*, **18**, 495–527.

Doswell, C. A. III, 2001: Severe convective storms—An overview. *Meteorological Monographs*, **28**, 1–26.

Doswell, C. A. III, and D.W. Burgess, 1993: Tornadoes and tornadic storms: a review of conceptual models. *The Tornado: Its Structure, Dynamics, Prediction, and Hazards*, *Geophys. Monogr.*, No. 79, Amer. Geophys. Union, 161-172.

Durran, D. R., P. A. Reinecke, and J. D. Doyle, 2013: Large-scale errors and mesoscale predictability in Pacific Northwest snowstorms. *J. Atmos. Sci.*, **70**, 1470–1487.

Durran, D. R., and M. Gingrich, 2014: Atmospheric predictability: why butterflies are not of practical importance. *J. Atmos. Sci.*, **71**, 2476–2488.

Gilmore, M. S., J. M. Straka, and E. N. Rasmussen, 2004: Precipitation and evolution sensitivity in simulated deep convective storms: Comparisons between liquid-only and simple ice and liquid phase microphysics. *Mon. Wea. Rev.*, **132**, 1897-1916.

Hohenegger, C., and C. Schär, 2007: Atmospheric predictability at synoptic versus cloud-resolving scales. *Bull. Amer. Meteor. Soc.*, **88**, 1783–1793.

Klemp, J. B., 1987: Dynamics of tornadic thunderstorms. *Ann. Rev. Fluid Mech.,* **19,** 369–402.

Klemp, J. B., and R. Rotunno, 1983: A study of the tornadic region within a supercell thunderstorm. *J. Atmos. Sci.*, **40**, 359–377.

Klemp, J. B., and R. B. Wilhelmson, 1978a: The simulation of three-dimensional convective storm dynamics. *J. Atmos. Sci.*, **35**, 1070–1096.

Klemp, J. B., and R. B. Wilhelmson, 1978b: Simulations of right- and left-moving storms produced through storm splitting. *J. Atmos. Sci.*, **35**, 1097–1110.

Lemon, L. R., and C. A. Doswell, 1979: Severe thunderstorm evolution and mesocyclone structure as related to tornadogenesis. *Mon. Wea. Rev.*, **107**, 1184–1197.

Lin, Y.-L., R. D. Farley, and H. D. Orville, 1983: Bulk parameterization of the snow field in a cloud model. *J. Climate Appl. Meteor.*, **22**, 1065–1092.

Lorenz, E., 1965: A study of the predictability of a 28-variable atmospheric model. *Tellus,* **17,** 321-333.

Lorenz, E., 1969: The predictability of a flow which possesses many scales of motion. *Tellus*, **21**, 289–307.

Lorenz, E., 1985: Atmospheric predictability experiments with a large numerical model. *Tellus*, **34**, 505-513.

Lorenz, E. N., 1996: Predictability— A problem partly solved. *Proc. Seminar on Predictability*, Vol. I, Reading, United Kingdom, ECMWF, 1-19.

Mansell, E. R., and C. L. Ziegler, 2013: Aerosol effects on simulated storm electrification and precipitation in a two-moment bulk microphysics model. *J. Atmos. Sci.*, **70**, 2032–2050.

Markowski, P. M., J. M. Straka, and E. N. Rasmussen, 2002: Direct surface thermodynamic observations within the rear-flank downdrafts of nontornadic and tornadic supercells. *Mon. Wea. Rev.*, **130**, 1692–1721.

Markowski, P. M., J. M. Straka, and E. N. Rasmussen, 2003: Tornadogenesis resulting from the transport of circulation by a downdraft: idealized numerical simulations. *J. Atmos. Sci.*, **60**, 795–823.

Markowski, P.M., and Y. P. Richardson, 2009: Tornadogenesis: our current understanding, forecasting considerations, and questions to guide future research. *Atmospheric Research*, **88**.

Markowski, P. M., and Y. P. Richardson, 2010: *Mesoscale Meteorology in Midlatitudes*. Wiley, 430 pp.

Naylor, J., M. A. Askelson, and M. S. Gilmore, 2012: Influence of low-level thermodynamic structure on the downdraft properties of simulated supercells. *Mon. Wea. Rev.*, **140**, 2575–2589.

Naylor, J., and M. S. Gilmore, 2014: Vorticity evolution leading to tornadogenesis and tornadogenesis failure in simulated supercells. *J. Atmos. Sci.*, **71**, 1201–1217.

Potvin, C. K., 2013: A variational method for detecting and characterizing convective vortices in Cartesian wind fields. *Mon. Wea. Rev.*, **141**, 3102–3115.

Rasmussen, Erik N., 2003: Refined Supercell and Tornado Forecast Parameters. *Wea. Forecasting*, **18**, 530–535.

Rasmussen, E. N., and D. O. Blanchard, 1998: A baseline climatology of sounding-derived supercell and tornado forecast parameters. *Wea. Forecasting*, **13**, 1148–1164.

Reinecke, P. A., D. Durran, 2009: The overamplification of gravity waves in numerical solutions to flow over topography. *Mon. Wea. Rev.*, **137**, 1533–1549.
Rotunno, R., 1981: On the evolution of thunderstorm rotation. *Mon. Wea. Rev.*, **109**, 577–586.

Rotunno, R., 1981: On the evolution of thunderstorm rotation. *Mon. Wea. Rev.*, **109**, 577–586.

Rotunno, R., and J. Klemp, 1985: On the rotation and propagation of simulated supercell thunderstorms. *J. Atmos. Sci.*, **42**, 271–292.

Schenkman, A. D., M. Xue, and A. Shapiro, 2012: Tornadogenesis in a simulated mesovortex within a mesoscale convective system. *J. Atmos. Sci.*, **69**, 3372–3390.

Schenkman, A. D., M. Xue, and M. Hu, 2014: Tornadogenesis in a high-resolution simulation of the 8 May 2003 Oklahoma City supercell. *J. Atmos. Sci.*, **71**, 130–154.

Stensrud, D. J., and Coauthors, 2009: Convective-scale Warn on Forecast: a vision for 2020. *Bull. Amer. Meteor. Soc.*, **90**, 1487–1499.

Stensrud, D. J., and Coauthors, 2013: Progress and challenges with Warn-on-Forecast. *Atmospheric Research.* **123**, 2-16

Stevens, B., C.-H. Moeng, and P. P. Sullivan, 1999: Large-eddy simulations of radiatively driven convection: sensitivities to the representation of small scales. *J. Atmos. Sci.*, **56**, 3963–3984.

Thompson, R. L., R. Edwards, J. A. Hart, K. L. Elmore, and P. Markowski, 2003: Close proximity soundings within supercell environments obtained from the Rapid Update Cycle. *Wea. Forecasting*, **18**, 1243–1261.

Thompson, R. L., B. T. Smith, J. S. Grams, A. R. Dean, and C. Broyles, 2012: Convective modes for significant severe thunderstorms in the contiguous United States. Part II: Supercell and QLCS tornado environments. *Wea. Forecasting*, **27**, 1136–1154.

Wicker, L. J., and R. B. Wilhelmson, 1993: Numerical simulation of tornadogenesis within a supercell thunderstorm. *The tornado: Its structure, dynamics, prediction, and hazards, Geophys. Monogr.*, No. 79, 75-88.

Wicker, L. J., and R. B. Wilhelmson, 1995: Simulation and analysis of tornado development and decay within a three-dimensional supercell thunderstorm. *J. Atmos. Sci.*, **52**, 2675–2703.

Wilhelmson, R. B., and J. B. Klemp, 1978: A numerical study of storm splitting that leads to long-lived storms. *J. Atmos. Sci.*, **35**, 1974–1986.

Yussouf, N., E. R. Mansell, L. J. Wicker, D. M. Wheatley, and D. J. Stensrud, 2013: The ensemble Kalman filter analyses and forecasts of the 8 May 2003 Oklahoma City tornadic supercell storm using single- and double-moment microphysics schemes. *Mon. Wea. Rev.*, **141**, 3388–3412.

Zhang, F., A. M. Odins, and J. W. Nielsen-Gammon, 2006: Mesoscale predictability of an extreme warm-season precipitation event. *Wea. Forecasting*, **21**, 146-166.

Appendix A: CM1 namelist file used for supercell simulations

```
&param0
 nx         =     1200,
 ny         =     1200,
 nz         =     106,
 nodex      =     100,
 nodey      =     75,
 timeformat =     1,
 timestats  =     1,
 terrain_flag = .false.,
 procfiles  = .false.,
 /

 &param1
 dx    = 100.0,
 dy    = 100.0,
 dz    =  200.0,
 dtl   =  0.5,
 timax = 10800.0,
 tapfrq =   30.0,
 rstfrq =   1500.0,
 statfrq =  5.0,
 prclfrq =  5.0,
 /

 &param2
 adapt_dt = 0,
 irst     = 0,
 rstnum   = 4500,
 iconly   = 0,
 hadvorder = 5,
 vadvorder = 5,
 pdscheme = 1,
 advweno  = 2,
 advwenouvw = 0,
 idiff    = 1,
 vdiff    = 0,
 mdiff    = 0,
 difforder = 6,
 imoist   = 1,
 iturb    = 1,
 tconfig  = 1,
 bcturbu  = 3,
 bcturbs  = 1,
 dns      = 0,
```

```
irdamp   = 1,
hrdamp   = 0,
psolver  = 3,
nsound   = 6,
ptype    = 29,
ihail    = 1,
iautoc   = 1,
icor     = 0,
pertcor  = 0,
neweqts  = 2,
idiss    = 1,
efall    = 0,
rterm    = 0,
wbc      = 2,
ebc      = 2,
sbc      = 2,
nbc      = 2,
irbc     = 4,
roflux   = 0,
isnd     = 7,
iwnd     = 2,
itern    = 0,
iinit    = 1,
irandp   = 0,
ibalance = 0,
iorigin  = 1,
axisymm  = 0,
imove    = 1,
iptra    = 0,
npt      = 1,
iprcl    = 0,
nparcels = 1,
/

&param3
kdiff2 =  75.0,
kdiff6 =  0.040,
fcor   = 0.00005,
kdiv   = 0.10,
alph   = 0.60,
rdalpha = 3.3333333333e-3,
zd     =  17000.0,
xhd    = 100000.0,
umove  =  8.0,
vmove  =  6.0,
v_t    =     7.0,
```

```
l_h    =  1000.0,
l_inf  =   100.0,
ndcnst =   250.0,
/

&param11
radopt =       0,
dtrad  =   300.0,
ctrlat =   36.68,
ctrlon =  -98.35,
year   =    2009,
month  =       5,
day    =      15,
hour   =      21,
minute =      38,
second =      00,
/

&param12
idrag     =     1,
isfcflx   =     0,
sfcmodel  =     0,
oceanmodel =    0,
ipbl      =     0,
initsfc   =     1,
tsk0      = 299.28,
tmn0      = 297.28,
xland0    =   2.0,
lu0       =    16,
season    =     1,
cecd      =     1,
pertflx   =     0,
cnstce    =  0.0104,
cnstcd    =  0.0104,
isftcflx  =     0,
iz0tlnd   =     0,
oml_hml0  =  50.0,
oml_gamma =  0.14,
/

&param4
stretch_x =     0,
dx_inner  =  1000.0,
dx_outer  =  7000.0,
nos_x_len =  40000.0,
tot_x_len = 120000.0,
```

```
/

&param5
stretch_y =      0,
dy_inner  =    1000.0,
dy_outer  =    7000.0,
nos_y_len =   40000.0,
tot_y_len =  120000.0,
/

&param6
stretch_z = 2,
ztop      =  21200.0,
str_bot   =      10.0, !not in use
str_top   =  6200.0,   !not in use
dz_bot    =    40.0,
dz_top    =    500.0,
/

&param7
bc_wind   = 1,
bc_temp   = 1,
ptc_top   = 250.0,
ptc_bot   = 300.0,
viscosity = 25.0,
pr_num    = 0.72,
/

&param8
var1      =   10.0,    !I/O Headroom in GB
var2      =   0.0,
var3      =   1500.0,  !height of center of bubble AGL
var4      =   1500.0,  !vertical bubble radius
var5      =   2500.0,  !height of top of the shear layer (m) <-------used in buoy study
var6      =   10.0,    !ORF uconst2, u at top of shear layer <-------used in buoy study
var7      =   10000.0, !bubble horiz. radius (from init3d.F)
var8      =   30000.0, !ric
var9      =   25000.0, !rjc
var10     =   3.0,     !bptpert SET TO ZERO FOR WFORCE
/

&param9
output_path      = './',
output_basename  = 'Geary_Pert001',
output_format    = 5,
output_filetype  = 3,
```

```
output_interp    = 0,
output_rain      = 1,
output_sws       = 1,
output_coldpool  = 1,
output_sfcflx    = 1,
output_sfcparams = 1,
output_sfcdiags  = 1,
output_zs        = 0,
output_zh        = 0,
output_basestate = 1,
output_th        = 1,
output_thpert    = 1,
output_prs       = 1,
output_prspert   = 1,
output_pi        = 0,
output_pipert    = 0,
output_rho       = 1,
output_rhopert   = 1,
output_tke       = 1,
output_km        = 1,
output_kh        = 1,
output_qv        = 1,
output_qvpert    = 0,
output_q         = 1,
output_dbz       = 1,
output_u         = 1,
output_upert     = 0,
output_uinterp   = 1,
output_v         = 1,
output_vpert     = 0,
output_vinterp   = 1,
output_w         = 1,
output_winterp   = 1,
output_vort      = 1,
output_uh        = 1,
output_pblten    = 0,
output_dissten   = 0,
output_radten    = 0,
/

&param10
stat_w        = 1,
stat_u        = 1,
stat_v        = 1,
stat_rmw      = 0,
stat_pipert   = 0,
```

```
 stat_prspert  = 1,
 stat_thpert   = 1,
 stat_q        = 1,
 stat_tke      = 1,
 stat_km       = 1,
 stat_kh       = 1,
 stat_div      = 1,
 stat_rh       = 1,
 stat_rhi      = 1,
 stat_the      = 1,
 stat_cloud    = 1,
 stat_sfcprs   = 1,
 stat_wsp      = 1,
 stat_cfl      = 1,
 stat_vort     = 1,
 stat_tmass    = 1,
 stat_tmois    = 1,
 stat_qmass    = 1,
 stat_tenerg   = 1,
 stat_mo       = 1,
 stat_tmf      = 1,
 stat_pcn      = 1,
 stat_qsrc     = 1,
 /

&nssl2mom_params
!  alphah = 0,   ! shape parameter of graupel
!  alphahl = 2.0, ! shape parameter of hail
   ccn     = 2.0e9, ! base ccn concentration
   imurain = 1,
   cnor    = 8.e6,
   cnoh    = 4.e4,

/
 &param_wforce
 wforceon     = .false.,
 wforceendtime= 600.0,
 wforceendval = 8.0,
 wforcealpha  = 0.5,
 wforcexrad   = 7000.0,
 wforceyrad   = 7000.0,
 wforcezrad   = 3000.0,
 wforcexctr   = 10000.0,
 wforceyctr   = 16000.0,
 wforcezctr   = 3000.0,
/
```